NASA TECHNICAL NOTE

NASA TN D-3046

EXPERIMENTAL FLUTTER STUDY OF A WING-FUSELAGE CONFIGURATION AT A MACH NUMBER OF 15.4 AND COMPARISON WITH THEORY

by Robert C. Goetz and John L. Sewall

Langley Research Center

Langley Station, Hampton, Va.

NATIONAL AERONAUTICS AND SPACE ADMINISTRATION • WASHINGTON, D. C. • OCTOBER 1965

NASA TN D-3046

EXPERIMENTAL FLUTTER STUDY OF A WING-FUSELAGE CONFIGURATION AT A MACH NUMBER OF 15.4 AND COMPARISON WITH THEORY

By Robert C. Goetz and John L. Sewall

Langley Research Center
Langley Station, Hampton, Va.

NATIONAL AERONAUTICS AND SPACE ADMINISTRATION

For sale by the Clearinghouse for Federal Scientific and Technical Information
Springfield, Virginia 22151 – Price $2.00

EXPERIMENTAL FLUTTER STUDY OF A WING-FUSELAGE CONFIGURATION AT A MACH NUMBER OF 15.4 AND COMPARISON WITH THEORY

By Robert C. Goetz and John L. Sewall
Langley Research Center

SUMMARY

An investigation was conducted in helium flow at a Mach number of 15.4 to provide hypersonic flutter data on a low-aspect-ratio, flexible, wing-fuselage configuration. The models were sting-mounted in the 24-inch-diameter leg of the Langley Mach 15 hypersonic aeroelasticity tunnel on a support system which simulated the free-flight condition by permitting symmetric freedoms of vertical translation and pitch. The fuselage was cylindrical with a semirigid spherically blunted nose-cone section, and the wing was a 73° clipped delta with a modified trailing edge and a slab airfoil section. The model geometry and mass distribution were held constant while the ratio of wing stiffness to fuselage stiffness was varied.

The results indicate that increasing the wing-to-fuselage frequency ratio from 0 to about 1.0 is destabilizing, whereas a further increase in frequency ratio is stabilizing. However, the flexible model never becomes as stable as the rigid-fuselage model over the test range of wing-to-fuselage frequency ratios. From these results the fuselage flexibility was concluded to be an important flutter parameter. The stiffness of the model support system was at a level low enough to have no measurable effects on the flutter characteristics of the models in the present investigation.

Flutter calculations for some of the models were performed by application of a flutter analysis based on the first four coupled symmetric modes and on quasi-steady aerodynamic theory for approximating aerodynamic forces acting on wing and fuselage. Calculated flutter-speed trends were similar to experimental trends but were higher by as much as about 80 percent. The lack of a sufficient number of flexible wing-fuselage modes prevents a true assessment of the aerodynamic approximations used in the analysis. The use of a combination of Newtonian theory for the fuselage nose cone and piston theory for the rest of the configuration resulted in essentially the same flutter solution as that obtained by using piston theory for the entire wing-fuselage combination.

INTRODUCTION

Methods for treating the flutter characteristics of wing-fuselage combinations at high speeds have been formulated analytically in references 1 to 3; however, corroborating experimental flutter studies of similar wing-fuselage combinations are very scarce. Most experimental hypersonic flutter studies (refs. 4 to 8) have been devoted to specific wing-shape effects such as airfoil shape, leading-edge sweep, thickness-chord ratio, and leading-edge bluntness. These studies have a limited application to designs of proposed hypersonic vehicles in which the fuselage and the wing are merged so that it is impractical to treat them as separate components. In such designs the complete wing-fuselage combination must be considered.

Accordingly, the present investigation was undertaken to provide experimental hypersonic-flutter data on a low-aspect-ratio, flexible, wing-fuselage configuration. The purpose of this investigation was to assess the importance of fuselage flexibility on the flutter characteristics of the wing-fuselage combination. The model configuration, tested in helium flow at a Mach number of 15.4, consisted of a body of revolution, or fuselage, with a centrally mounted wing. The fuselage was cylindrical with a spherically blunted nose-cone section, and the wing was a 73° clipped delta with a modified trailing edge and a slab airfoil section. Models of this configuration were sting-mounted on a support system that simulated the free-flight condition by permitting symmetric freedoms of vertical translation and pitch. The primary variable of this investigation was the wing-to-fuselage stiffness ratio.

A coupled-mode flutter analysis based on quasi-steady aerodynamic theory was applied to models for which measured mode shapes were available, and comparisons are made between calculated and measured flutter results. Both piston theory and Newtonian theory were used to approximate the oscillating aerodynamic forces acting on wing and fuselage, and wing-fuselage aerodynamic interference effects were neglected.

SYMBOLS

A_{ij} aerodynamic coefficient in flutter analysis (see eqs. (A3) and (A5))

a speed of sound, feet per second

b_o wing reference semichord, 0.642 foot for all models (see fig. 1)

C_A axial-force coefficient, $\frac{\text{Axial force}}{q l_M^2}$

$C_L = \alpha C_{L_\alpha}$

C_{L_α} lift-curve slope

C_l rolling-moment coefficient, $\frac{\text{Rolling moment}}{q l_M^2 r_c}$

C_m pitching-moment coefficient about nose of model, $\frac{\text{Pitching moment}}{q l_M^2 l_F}$

C_N normal-force coefficient, $\frac{\text{Normal force}}{q l_M^2}$

F series defined by equation (A4)

f frequency, $\frac{\omega}{2\pi}$, cycles per second

g structural damping coefficient in flutter eigenvalue (see section of appendix following eq. (A1))

h_i, h_j normalized mode shape for ith and jth mode, respectively

i, j integers identifying modes used in analysis

k reduced frequency, $\frac{b_o \omega}{V}$

l_M reference length of model, 1.75 feet for all models

l_F fuselage length, $l_x \bar{l}_F$

l_x reference length in x-direction, $2b_o$ in the present paper

l_N length of fuselage nose cone including rounded nose, $l_x \bar{l}_N$, 0.521 foot for all models

M Mach number

M_i generalized mass in ith mode (see eq. (A2))

m_t total mass, slugs

m_F mass of fuselage per unit length

m_W mass of wing per unit area

q dynamic pressure

r radius of fuselage at any chordwise station, $l_x \bar{r}$

r_c radius of cylindrical fuselage section, $l_x\bar{r}_c$, 0.125 foot for all models

s wing semispan measured from fuselage center line

t local airfoil thickness

V velocity, feet per second

x chordwise coordinate, positive rearward, measured from fuselage nose, $l_x\bar{x}$

y spanwise coordinate, measured from model center line, $s\bar{y}$

α angle of attack (positive nose up), degrees

γ ratio of specific heats, 5/3 for helium (see eqs. (A3) and (A4))

δ semivertex angle of fuselage nose cone, 12 degrees

θ angle between local tangent to fuselage surface and longitudinal axis of fuselage

$\kappa_i = \frac{\pi\rho b_o^2 l_x}{M_i}$ (see section of appendix following eq. (A1))

μ mass-ratio parameter, $\frac{m_t}{\rho l_M^3}$

ρ density, slugs per cubic foot

Ω complex flutter eigenvalue, $\left(\frac{\omega_r}{\omega}\right)^2(1 + ig)$, (see section of appendix following eq. (A1))

ω angular frequency, $2\pi f$, radians per second

ω_r reference frequency, radians per second

$\left(\frac{\omega_W}{\omega_s}\right)^2$ flexible-to-rigid wing-mounting stiffness ratio, or wing-flapping stiffness ratio

$\frac{\omega_W}{\omega_4}$ wing-to-fuselage frequency ratio

$\left(\frac{\omega_W}{\omega_4}\right)^2$ wing-to-fuselage stiffness ratio

$\frac{V}{l_M \omega_W \sqrt{\mu}}$ flutter-speed-index parameter

Subscripts:

ac aerodynamic center, measured from model nose, fraction of model length

cg center of gravity, measured from nose, fraction of model length

f pertaining to flutter mode

s pertaining to wing mounted on rigid support

W pertaining to uncoupled wing flapping mode

A pertaining to wings mounted on body with bending stiffness A

B pertaining to wings mounted on body with bending stiffness B

C pertaining to wings mounted on body with bending stiffness C

A bar over a symbol denotes a nondimensional quantity.

EXPERIMENTAL PROGRAM

Description of Models

The model configuration tested in the present investigation consisted of a body of revolution with a centrally mounted wing which had a rounded leading edge swept 73° and a slab airfoil section. The model geometry is shown in figure 1. The fuselage consisted of a semirigid spherically blunted nose-cone section which had integral longitudinal inserts along the wing plane. These inserts extended back from the nose-cone section to constitute the main longitudinal bending stiffness of the flexible portion of the fuselage. A coil spring was wound through, and brazed to, the inserts in order to form a cylindrical body without contributing significant additional longitudinal bending stiffness. The coil spring was covered with a layer of rubber (dental dam) in order to provide a relatively smooth aerodynamic surface. In figures 2(a) to 2(d) the model can be seen in the various stages of construction.

The wing planform was a 73° clipped delta with a modified trailing edge. The wing was constructed of balsa wood with two steel flexure-beam inserts oriented in the spanwise direction. The exposed portion of flexure beams was 3/16 inch wide and 1/8 inch long, and the thickness was varied in order to change the wing flapping stiffness. These flexure beams were bolted to the integral longitudinal inserts at two fuselage stations. (See fig. 2(e).) Model geometry and mass distribution were held constant while the ratio of wing stiffness to fuselage stiffness was varied. A rigid-fuselage model was constructed,

with the wings connected in the same manner as they were on the flexible model, in order to assess the effect of fuselage flexibility on the flutter characteristics. Figure 2(f) shows the rigid-fuselage model with the upper portion of the cylindrical fuselage rotated out of place.

Each model is designated by a capital letter, an integer, and a lower case letter. The capital letter indicates the level of the fuselage longitudinal bending stiffness: A is stiffer than B, and C is rigid. The integer indicates the level of wing flapping stiffness: $5 > 4 > 3 > 2 > 1$. The lower-case letter indicates the level of model support stiffness: $a > b > c$. For example, C-1-c means that the fuselage is rigid, the wing flapping stiffness is the weakest, and the model support system is the weakest.

Model Support System

The models were sting mounted in the tunnel on a flexure-pivot support system. The support system consisted of a pair of parallel flexure springs clamped on the sting, with a cross-pivot spring connected to the free ends. The free end of the cross-pivot spring was connected to the model by a vertical rigid rectangular shaft. Figure 3 shows a view of the model support system partially assembled. Three levels of support-system stiffness were used in order to determine whether the support system was in any way influencing, or contributing to, the model flutter characteristics. At all three levels the system had a translation-to-pitch frequency ratio of about 2/3.

Physical Properties

The total mass (excluding the mass of the model support system) and natural frequencies of the various models are listed in table I(a). The weight distribution of the model support system is shown in figure 4(a). Figure 4(b) shows the weight distribution, obtained by weighing the various model components, for a typical flexible fuselage. A typical measured wing-weight distribution is presented in figure 4(c); this distribution was determined by cutting the wing chordwise and spanwise as indicated in the numbered pattern in figure 5 and weighing each segment. It should be noted that figure 4(c) also includes a table of the concentrated mass for each wing due to the steel flexure beams which extend over the entire wing span at their appropriate chordwise stations. The difference between the total mass of the rigid- and flexible-body models as shown in table I(a) was in the cylindrical portion of the fuselage, and was uniformly distributed. This difference changes the location of the model center of gravity as is shown in figure 5. The cross-pivot location (pitch axis) of the support system was $0.415l_M$ (measured from the nose) for all models.

All models were vibrated on the model support system with an interrupted-air-jet shaker to determine their natural frequencies and mode shapes. Mode shapes were measured by using a pivoted-coil-galvanometer element whose output was recorded on an oscillograph while the models were vibrating with constant amplitude in their natural modes. These displacement measurements were taken at various stations on the model (circled coordinates in fig. 5), and the

results were normalized with respect to maximum displacement in a given mode. These results for several of the models are presented in figures 6 to 9. A brief summary of the model motion in each given mode follows:

(1) First mode (model translation) - The model behaved essentially as a rigid body with vertical translation predominating.

(2) Second mode (model pitch) - The model behaved essentially as a rigid body with pitching predominating.

(3) Third mode (model rolling) - The model oscillated about the model center line in an antisymmetric fashion. This antisymmetric mode has not been included in figures 6 to 9 because it was not regarded as contributing to the symmetric flutter motion.

(4) Fourth mode (fuselage bending) - The fuselage had a definite deformation along its length, and the wing motion was symmetric but out of phase with the fuselage motion. (The omission of this mode in fig. 8 is due to the rigidity of the fuselage for model C-1-a.)

(5) Fifth mode (wing-fuselage combination) - The maximum displacement occurs at the wing tip. The wing motion is symmetric but out of phase with the fuselage motion. The wing is relatively rigid over its span, whereas the fuselage is flexible.

In addition to the foregoing coupled modes, an uncoupled mode was measured in order to investigate the effect of wing flapping stiffness. The fuselage was restrained along two planes tangent to its upper and lower cylindrical surfaces, while the wing flapping displacement was measured. The frequency of this mode was lower than that obtained with the wing flexure beam fastened to a rigid support, because the wing-fuselage junction could take on deformations. For comparison, the frequency of each wing mounted on a rigid support and on the various flexible fuselages is listed in table I(b). This table includes some geometric details of the wing flexure beams and shows the amount of stiffness reduction due to the flexible wing-fuselage junction. These data are presented in figure 10, where it can be seen that the wing-flapping stiffness ratio for the wing mounted on the flexible bodies with stiffness levels A and B is about 25 and 50 percent lower, respectively, than for the same wing mounted on the rigid body.

Wind-Tunnel-Test Procedure

The tests were performed in the 24-inch-diameter leg of the Langley Mach 15 hypersonic aeroelasticity tunnel, which uses helium as a test medium. This tunnel has a contoured nozzle designed to generate a uniform flow at a Mach number of about 15. A description of this facility and its operating characteristics can be found in reference 8.

Models were sting mounted in the tunnel at zero angle of attack. The tunnel with its vacuum reservoir was then evacuated to a pressure of 1/2 inch of

mercury absolute. A control valve upstream of the test section was opened, and flow was established at a dynamic pressure of about 100 lb/sq ft. The dynamic pressure was held constant for about 1.5 seconds so that the model transient motion could die out. Then with the Mach number remaining constant, the dynamic pressure was increased until either flutter was encountered or the maximum tunnel operating conditions were reached. The average total running time for these tests was about 5 seconds.

Throughout the tests, stagnation temperature and pressure were recorded on an oscillograph together with signals from resistance-type strain gages mounted on the model support system, on the fuselage longitudinal inserts, and on the wing flexure beams so that the tunnel conditions could be correlated with the model behavior. Flow conditions in the test section were obtained from the stagnation pressure and temperature by assuming isentropic nozzle flow at the appropriate Mach number. The start of flutter and the flutter frequency were determined from the strain-gage response. Fouling switches were mounted on the model at appropriate locations to indicate when the amplitude reached a value high enough to cause the model to hit the sting. High-speed motion pictures were taken of the behavior of most of the models during the tests.

As part of the experimental program concerning this configuration, the steady aerodynamic forces and moments were obtained by using an internal strain-gage balance mounted in a rigid-body model. A photograph of the model, with the upper half of the cylindrical portion of the fuselage removed, and of the strain-gage balance can be seen in figure 11.

METHOD AND APPLICATION OF FLUTTER ANALYSIS

A Rayleigh-Ritz, coupled-mode flutter analysis, such as that described on page 555 of reference 9, was applied to four of the models tested in this study and having a wide variation in wing-to-fuselage frequency ratio. The measured-mode-shape data for modes 1, 2, 4, and 5 are presented in figures 6 to 9. The third mode was not considered because it was antisymmetric and therefore not involved in a study of symmetric flutter.

The determinantal flutter equation used for the flutter calculations is given in the appendix. The integrals in the expressions for the generalized mass and aerodynamic coefficients were evaluated numerically by using spanwise coordinates 1, 2, 3, and 4 in figure 5, with the chordwise integrands fitted to eighth-degree polynomials based on nine equally spaced stations including stations on the leading and trailing edges. The generalized mass was based on the distribution of masses per unit area calculated from the known weights and volumes of the materials used in the construction of the model. The contributions from the model support system and flexure beams joining the wing to the body were treated additionally as concentrated masses.

The generalized aerodynamic coefficients given in the appendix are based on the quasi-steady aerodynamic approaches of piston theory and Newtonian theory. Two applications of these theories were used; one involved the use of

piston theory for both wing and fuselage; the other differed from the first only in the use of Newtonian theory on the fuselage-nose-cone frustum. Wing-fuselage aerodynamic interference effects were not considered. Some calculations of the quasi-steady generalized aerodynamic section forces based on Newtonian theory as applied to the rounded leading edge of the wing indicated negligible contributions of the forces acting on this surface in comparison with the piston-theory generalized aerodynamic forces acting on the rest of the wing section. As a result of the negligible effect indicated by these calculations, a separate approximation of the forces acting on the rounded leading edge of the wing was not included in the flutter calculations presented in the paper. Steady Newtonian aerodynamic forces acting on the spherically blunted nose cap of the fuselage were also found to be negligible in comparison with those acting on the rest of the nose-cone section. Consequently, a separate approximation of the forces acting on the nose cap was also omitted in the flutter calculations.

RESULTS AND DISCUSSION

Experimental Results

The results of the wind-tunnel flutter tests are presented in table II, which includes a list of the flow conditions at flutter as well as the flutter frequency ratio ω_f/ω_W and the flutter-speed-index parameter $V/l_M\omega_W\sqrt{\mu}$ for each test run. Two of the models tested did not encounter flutter; the data given for the models are for the maximum tunnel conditions reached during the run. Experimental results from table II are presented in figures 12 and 13 as variations of flutter-speed-index parameter and of frequency ratio ω/ω_W with wing-to-fuselage frequency ratio ω_W/ω_4.

The data represented by circles in figure 12 show a flutter speed trend for the system in which the frequency ratio has been varied from 0.677 to 1.508, while the fuselage stiffness remained constant. This trend indicates that increasing the frequency ratio from 0.677 to about 1.0 is destabilizing, whereas increasing it further, at least to 1.508, is stabilizing. The same general trend was obtained when the fuselage longitudinal bending stiffness was varied as is shown by the data indicated by the square symbols in figure 12. A rigid-fuselage model was tested in order to extend the frequency ratio to zero, and the data indicated by the diamond symbols in figure 12 show that its flutter-speed-index parameter is almost 60 percent higher than that of the flexible model with the lowest frequency ratio (0.677). The flutter-speed-index parameter of the flexible models is always lower than that of the rigid model over the range of frequency ratios in the investigation; thus, the flexible model never becomes as stable as the rigid-fuselage model. These results show that fuselage flexibility is an important flutter parameter and definitely indicate the need for simulating fuselage flexibility in flutter studies of this type of configuration.

The data represented in figure 12 by ticked symbols are for models that were retested after the support-system stiffness had been reduced. The symbols with flags represent data obtained at stiffness level b (stiffness 30 percent of original value) and the symbols with tails, data obtained at stiffness level c (stiffness 15 percent of original value). The consistency of the flutter-speed results, regardless of the support-system stiffness used, indicates that the original support-system-stiffness level was low enough to simulate the free-flight condition; that is, the support-system rigid-body frequencies were far enough removed from the frequencies of the elastic modes of the model so that they would not influence, or contribute to, the instability of the model.

In figure 13 the flutter frequency as well as the system natural frequencies, all normalized to the wing flapping frequency, are presented for all models tested. The flutter frequency ratio is relatively constant over the range of parameters of this investigation. The flutter motion is a coupled wing-to-fuselage symmetric mode that changes from being predominantly the fourth to predominantly the fifth natural mode for wing-to-fuselage frequency ratios greater than about 0.95.

As part of the experimental program for this configuration the normal force, axial force, rolling moment, and pitching moment were measured on a rigid-fuselage model at angles of attack of 4° and 10°. These results are presented in coefficient form in table III which also includes the aerodynamic-center location. Also included in the table are theoretical values for the coefficients of normal force and pitching moment about the nose of the model, the location of the aerodynamic center, and other pertinent quantities for the same configuration. These theoretical forces were determined by using the following combination of piston theory and Newtonian theory. Newtonian theory was applied to the rounded leading edge of the wing, to the spherically blunted nose of the fuselage, and to the fuselage cone frustum. Piston theory was applied to the planar surfaces of the wing and to the cylindrical portion of the fuselage. Shown in table III are the differences between the experimental and theoretical forces and moments expressed as percents of the experimental values. These differences are believed to be due to the wing and fuselage aerodynamic forces being derived independently without consideration of any wing-fuselage interference effects.

Theoretical Flutter Results and Comparison with Experiment

The flutter speeds and flutter frequencies calculated by means of the coupled-mode flutter equation given in the appendix are plotted in dimensionless form along with the experimental flutter speeds and flutter frequencies in figures 12 and 13. The flutter calculations were made for the four models whose mode shapes are presented in figures 6 to 9. The natural frequencies given in these figures for models A-2-a, B-4-a, C-1-a, and A-2-c correspond to those given in table I(a) for runs 34, 32, 33, and 37, respectively. Additional flutter calculations were made for runs 27, 28, and 31. The mode shapes of model A-2-a in figure 6 were assumed to correspond to the natural frequencies listed in table I(a) for runs 27 and 28, and the mode shapes of model B-4-a in figure 7 were assumed to correspond to the natural frequencies for run 31.

The theoretical results in figures 12 and 13 are based on piston theory for the wings and cylindrical fuselage section and on Newtonian theory for the fuselage nose-cone frustum. These results were changed by an insignificant amount when piston theory was used for all lifting surfaces on the configuration.

From figure 12 it is evident that the theory predicts flutter speed trends that are somewhat similar to the experimental trends but are unconservative - that is, above experimental trends by about 3 percent to 80 percent. Figure 13 shows the theoretical flutter frequencies to be in better agreement with experimental flutter frequencies at wing-to-fuselage frequency ratios near 0.8 than for wing-to-fuselage frequency ratios of 0 and above 0.8. It should be noted that the values of ω_W/ω_4 at which the agreement between theory and experiment is poorest are those for which the fifth-mode frequencies, which were the highest measured in this study, approach the experimental flutter frequencies. As the spread between these two upper frequencies increases, the theoretical and experimental flutter frequencies tend to approach one another. These frequency comparisons indicate the need for additional higher order modes having greater flexibility than that indicated in figures 6 to 9, particularly in the chordwise direction on the wing. Unfortunately, the models were destroyed during flutter before the flutter calculations were made and before the need for more modes was recognized.

Without the knowledge of additional modes it is impossible to tell whether the theoretical flutter-speed trends in figure 12 correspond to converged solutions, although all the natural modes available were used and found to be needed to obtain these trends. For example, in some calculations not presented herein, omission of the fourth mode resulted in a 69-percent increase in flutter speed and a 76-percent decrease in flutter frequency for model A-2-a at $\frac{\omega_W}{\omega_4} = 0.800$ (run 34). Thus, with the limited number of natural modes available, the adequacies of the quasi-steady aerodynamic approximations involved in the flutter mode cannot be truly assessed for the configuration. It can simply be noted that such aerodynamic approximations do not account for the actual flow field between the strong shock wave and the body surfaces, a fact which may well be important.

CONCLUDING REMARKS

A wind-tunnel investigation was conducted in helium flow at a Mach number of 15.4 to provide hypersonic flutter data on a low-aspect-ratio, flexible, wing-fuselage configuration, and the results are compared with the results of flutter calculations. The models were sting mounted in the 24-inch-diameter leg of the Langley Mach 15 hypersonic aeroelasticity tunnel on a support system which simulated the free-flight condition by allowing symmetric freedoms of vertical translation and pitch. The fuselage was cylindrical with a spherically blunted nose-cone section, and the wing was a 73° clipped delta with a modified trailing edge and a slab airfoil section. Model geometry and mass

distribution were held constant while the ratio of wing stiffness to fuselage stiffness was varied.

The experimental results indicate a destabilizing flutter-speed trend when the wing-to-fuselage frequency ratio is increased from 0 to about 1.0. The trend becomes stabilizing when the frequency ratio is increased to values greater than 1.0, but the flutter-speed-index parameter of the flexible models is always lower than that of the rigid model over the range of wing-to-fuselage frequency ratios in this investigation. The results further show that the flutter frequency ratio is relatively constant over this same range, and that the flutter motion is a coupled wing-fuselage symmetric mode. The fact that the flutter speed did not appear to be influenced by wide variations in the support system stiffness indicates that the original support-system-stiffness level was low enough to simulate the symmetric free-flight conditions of vertical translation and pitch. The conclusion reached from the experimental flutter results is that fuselage flexibility is an important flutter parameter and that flutter speeds of a rigid-fuselage model can be unconservative, or higher, than those of a flexible-fuselage model.

Flutter calculations based on the first four measured coupled modes and on quasi-steady aerodynamic forces determined by using a combination of piston theory and Newtonian theory gave flutter-speed trends similar to experimental trends but anywhere from about 3 percent to 80 percent higher. The possibility of better correlation between theory and experiment suffers from lack of higher order, flexible, wing-fuselage modes with which to approximate the analytical flutter mode more accurately and thereby assess the aerodynamic approximation more fully. The highly simplified representation of the unsteady aerodynamic forces acting on wing and fuselage, with wing-fuselage interference effects neglected, is another possible cause of the discrepancy between flutter theory and experiment. The use of Newtonian theory for the fuselage nose-cone frustum and piston theory for the wing and cylindrical fuselage section resulted in essentially the same flutter solution as that obtained by using piston theory for all lifting surfaces on the configuration.

Langley Research Center,
National Aeronautics and Space Administration,
Langley Station, Hampton, Va., June 8, 1965.

APPENDIX

COUPLED-MODE FLUTTER EQUATION FOR WING-FUSELAGE CONFIGURATION SUBJECTED TO QUASI-STEADY AERODYNAMIC LOADING

The theoretical flutter-speed and flutter-frequency trends shown in figures 12 and 13 were calculated by solution of the following determinantal coupled-mode flutter equation (based on p. 555 of ref. 9):

$$\begin{vmatrix} 1 - \left(\frac{\omega_1}{\omega_r}\right)^2 \Omega + \frac{\kappa_1}{k^2} A_{11} & \frac{\kappa_1}{k^2} A_{12} & \cdot & \cdot \\ \frac{\kappa_2}{k^2} A_{21} & 1 - \left(\frac{\omega_2}{\omega_r}\right)^2 \Omega + \frac{\kappa_2}{k^2} A_{22} & \cdot & \cdot \\ \cdot & \cdot & \cdot & \cdot \\ \cdot & \cdot & & 1 - \left(\frac{\omega_i}{\omega_r}\right)^2 \Omega + \frac{\kappa_i}{k^2} A_{ii} \end{vmatrix} = 0 \quad (A1)$$

where $\Omega = \left(\frac{\omega_r}{\omega}\right)^2 (1 + ig)$ in terms of reference frequency ω_r and structural damping coefficient g, and where $\kappa_i = \frac{\pi \rho b_o^2 l_x}{M_i}$ in terms of gas density ρ, wing root semichord b_o, reference length l_x, and generalized mass M_i which is given by

$$M_i = \frac{1}{2} \int_0^{l_F} m_F(x)\, h_i^2(x)\, dx + \iint_S m_W(x,y)\, h_i^2(x,y)\, dx\, dy \quad (i = 1, 2, \ldots) \quad (A2)$$

The first integral in this equation represents the fuselage contribution and the second integral $\left(\iint_S = \text{surface integral}\right)$, the wing contribution to the ith generalized mass. The mode shape is denoted by h_i; the fuselage mass per unit length, by m_F; the wing mass per unit area, by m_W; and the fuselage length, by l_F.

APPENDIX

A_{ij} in equation (A1) denotes the general term for the aerodynamic coefficients which are also made up of two integrals consistent with the linear superposition of forces on the wing and fuselage and the neglect of aerodynamic interference effects between the two. With the application of piston theory for both wing and fuselage (based on refs. 10 and 11), the general expression for A_{ij} is

$$A_{ij} = -\frac{1}{2M}\int_0^{\bar{l}_F} F\bar{r}h_i\left(\frac{dh_j}{d\bar{x}} + i\frac{l_x}{b_o}kh_j\right)d\bar{x} - \frac{2}{M\pi}\frac{s}{l_x}\iint_S h_i\left(\frac{\partial h_j}{\partial\bar{x}} + i\frac{l_x}{b_o}kh_j\right)d\bar{x}\,d\bar{y}$$

$$-\frac{\gamma+1}{2\pi}\frac{s}{l_x}\iint_S h_i\frac{dt}{dx}\left(\frac{\partial h_j}{\partial\bar{x}} + i\frac{l_x}{b_o}kh_j\right)d\bar{x}\,d\bar{y} \quad (i, j = 1, 2, \ldots) \quad (A3)$$

where $k = \frac{b_o\omega}{V}$, $x = l_x\bar{x}$, $l_F = l_x\bar{l}_F$, and $y = s\bar{y}$ and where r is the fuselage radius with $r = l_x\bar{r}$, s is the wing semispan measured from the model center line, γ is the ratio of specific heats, and t is the local airfoil thickness. The quantity F (based on ref. 10) is

$$F\left(M,\gamma,\frac{dr}{dx}\right) = 1 + \frac{\gamma+1}{2}\left(M\frac{dr}{dx}\right) + \frac{\gamma+1}{4}\left(M\frac{dr}{dx}\right)^2 + \ldots \quad (A4)$$

(It should be noted that the presence of all positive signs in equation (A4) in contrast with the alternating signs in equation (3.6) in reference 10 is due to the difference in sign convention between the present analysis and that of reference 10; in the present analysis the coordinate x is considered positive rearward in the same direction as the flow.)

For the present configuration (cone-cylinder fuselage and slab-airfoil-section wing) equation (A3) becomes

$$A_{ij} = -\frac{F}{2M}\left[\tan\delta\int_0^{\bar{l}_N} h_i\left(\bar{x} - \bar{l}_N\right)\left(\frac{dh_j}{d\bar{x}} + 2ikh_j\right)d\bar{x} + \bar{r}_c\int_0^{\bar{l}_N} h_i\left(\frac{dh_j}{d\bar{x}} + 2ikh_j\right)d\bar{x}\right] - \frac{\bar{r}_c}{2M}\int_{\bar{l}_N}^{\bar{l}_F} h_i\left(\frac{dh_j}{d\bar{x}} + 2ikh_j\right)d\bar{x}$$

$$-\frac{1}{M\pi}\frac{s}{b_o}\iint_S h_i\left(\frac{\partial h_j}{\partial\bar{x}} + 2ikh_j\right)d\bar{x}\,d\bar{y} \quad (A5)$$

where $\bar{r} = \left(\bar{x} - \bar{l}_N\right)\tan\delta + \bar{r}_c$ in terms of the cone semivertex angle δ, the dimensionless fuselage cylinder radius $\bar{r}_c$, and the dimensionless location of the juncture between the fuselage nose cone and cylinder $\bar{l}_N$. The reference length l_x is chosen as $2b_o$ (see fig. 1), and all values of x and r are referred to this length. Because of the slab airfoil section $\frac{dt}{dx} = 0$ and, therefore, the last integral in equation (A3) disappears. In the equation for F (eq. (A4)) dr/dx is simply $\tan\delta$.

With the introduction of Newtonian theory for the fuselage (ref. 12), the first integral in equation (A3) is replaced by

$$-\frac{1}{2}\int_0^{\bar{l}_F} h_i \bar{r} \sin 2\theta \left(\frac{dh_j}{d\bar{x}} + i\,\frac{l_x}{b_o}\,kh_j\right) d\bar{x} \tag{A6}$$

where θ is the angle between the local tangent to the surface of the fuselage and the longitudinal axis of the fuselage.

The introduction of Newtonian theory to the flutter analysis of the present wing-fuselage configuration affects only the first two integrals in equation (A5). With F/M omitted, these integrals are replaced by

$$-\sin^2\delta \int_0^{\bar{l}_N} h_i\left(\bar{x} - \bar{l}_N\right)\left(\frac{dh_j}{d\bar{x}} + 2ikh_j\right) d\bar{x} - \frac{\bar{r}_c}{2}\sin 2\delta \int_0^{\bar{l}_N} h_i\left(\frac{dh_j}{d\bar{x}} + 2ikh_j\right) d\bar{x} \tag{A7}$$

Separate integrations over the blunt leading edges of the fuselage and wing were omitted inasmuch as the contributions from these integrals were considered insignificant in comparison with contributions from the other integrals.

REFERENCES

1. Rodden, William P.; Farkas, Edith F.; and Malcom, Heather A.: Flutter and Vibration Analysis by a Modal Method: Analytical Development and Computational Procedure. Rept. No. TDR-169(3230-11)TN-15 (SSD-TDR-63-158), Aerospace Corp. (El Segundo, Calif.), July 31, 1963.

2. Rodden, William P.; Farkas, Edith F.; and Malcom, Heather A.: Flutter and Vibration Analysis by a Collocation Method: Analytical Development and Computational Procedure. Rept. No. TDR-169(3230-11)TN-14 (SSD-TDR-63-157), Aerospace Corp. (El Segundo, Calif.), July 31, 1963.

3. Yates, John E.: Supersonic Flutter of Airframes With Flexible Bodies. Contract NOw 62-0099-d, Midwest Res. Inst., Dec. 31, 1962.

4. Doggett, Robert V., Jr.: Experimental Flutter Investigation of Some Simple Models of a Boost-Glide-Vehicle Wing at Mach Numbers of 3.0 and 7.3. NASA TM X-37, 1959.

5. Goetz, Robert C.: Effects of Leading-Edge Sweep on Flutter Characteristics of Some Delta-Planform Surfaces at a Mach Number of 15.4. NASA TN D-2360, 1964.

6. Young, Lou S.: Effects of Angle of Attack and Thickness Ratio on the Flutter of a Rigid Unswept Diamond-Airfoil-Section Wing at a Mach Number of 10.0. NASA TN D-1380, 1962.

7. Hanson, Perry W.: Aerodynamic Effects of Some Configuration Variables on the Aeroelastic Characteristics of Lifting Surfaces at Mach Numbers From 0.7 to 6.86. NASA TN D-984, 1961.

8. Goetz, Robert C.: Effects of Leading-Edge Bluntness on Flutter Characteristics of Some Square-Planform Double-Wedge Airfoils at a Mach Number of 15.4. NASA TN D-1487, 1962.

9. Bisplinghoff, Raymond L.; Ashley, Holt; and Halfman, Robert L.: Aeroelasticity. Addison-Wesley Pub. Co., Inc., c.1955.

10. Miles, J. W.; and Young, Dana: Generalized Missile Dynamics Analysis. III - Aerodynamics. GM-TR-0165-00360, Space Technol. Lab., The Ramo-Wooldridge Corp., Apr. 7, 1958.

11. Ashley, Holt; and Zartarian, Garabed: Piston Theory - A New Aerodynamic Tool for the Aeroelastician. Jour. of Aero. Sci., vol. 23, no. 12, Dec. 1956, pp. 1109-1118.

12. Grimminger, G.; Williams, E. P.; and Young, G. B. W.: Lift on Inclined Bodies of Revolution in Hypersonic Flow. J. Aeron. Sci., vol. 17, no. 11, Nov. 1950, pp. 675-690.

TABLE I.- MODEL PROPERTIES

(a) Mass and frequency

Model	Run	Model mass, slug	Frequencies, cps						Angular frequencies, rad/sec		$\left[\frac{\omega_W}{\omega_4}\right]^2$	$\frac{\omega_W}{\omega_4}$
			f_1	f_2	f_3	f_4	f_W	f_5	ω_W	ω_4		
A-1-a	29	0.0294	7.2	10.5	13.0	24.0	16.3	29.3	102.4	150.8	0.46	0.679
A-2-a	34	.0294	7.3	10.5	12.0	25.0	20.0	29.0	125.7	157.1	.64	.800
A-3-a	27	.0294	7.0	10.0	12.5	27.5	24.0	32.0	150.8	172.8	.76	.873
A-4-a	28	.0294	7.3	10.9	13.0	26.8	33.0	38.5	207.3	168.4	1.52	1.231
A-5-a	30	.0294	7.4	10.9	13.0	26.0	39.2	----	246.3	163.4	2.27	1.507
B-4-a	32	.0294	7.1	10.7	12.5	20.0	26.5	31.0	166.5	125.7	1.76	1.325
B-5-a	31	.0294	7.4	10.9	13.3	20.0	30.0	37.0	188.5	125.7	2.25	1.500
A-2-b	36	.0294	4.0	6.0	9.5	24.7	19.5	30.0	122.5	155.2	.62	.789
A-2-c	37	.0294	2.6	4.0	8.0	24.0	19.0	27.0	119.4	150.8	.63	.792
C-1-a	33	.0263	6.7	11.0	13.8	$\rightarrow\infty$	19.4	24.0	121.9	$\rightarrow\infty$	0	0
C-1-b	35	.0263	5.0	8.9	12.8	$\rightarrow\infty$	19.0	23.0	119.4	$\rightarrow\infty$	0	0

(b) Wing-flapping-stiffness details

Model	Flexure-beam thickness, in.		Frequencies, cps				Stiffness ratios		
	Front	Rear	f_s	$f_{W,C}$	$f_{W,A}$	$f_{W,B}$	$\left(\frac{\omega_{W,A}}{\omega_s}\right)^2$	$\left(\frac{\omega_{W,B}}{\omega_s}\right)^2$	$\left(\frac{\omega_{W,C}}{\omega_s}\right)^2$
A-1-a	0.012	0.016	20.90		16.25		0.605		
C-1-a	.012	.016	20.90	19.40					0.862
C-1-b	.012	.016	20.90	19.00					.828
A-2-a	0.014	0.018	25.00		20.00		0.640		
A-2-b	.014	.018	25.00		19.50		.609		
A-2-c	.014	.018	25.00		19.00		.578		
A-3-a	0.016	0.020	31.25		24.00		0.590		
A-4-a	0.020	0.025	42.00		33.00		0.618		
B-4-a	.020	.025	42.00			26.50		0.398	
A-5-a	0.025	0.032	51.70		39.20		0.576		
B-5-a	.025	.032	51.70			30.00		0.337	

TABLE II.- EXPERIMENTAL FLUTTER RESULTS

$[l_M = 1.75 \text{ ft}]$

Model	Run	q, lb/sq ft	ρ, slugs/cu ft	a, ft/sec	V, ft/sec	M	ω_w, rad/sec	μ	$\frac{V}{l_M \omega_w \sqrt{\mu}}$	ω_f, rad/sec	$\frac{\omega_f}{\omega_w}$
A-1-a	29	150	0.0658×10^{-4}	450	6750	15.0	102.0	834	1.31	133.5	1.30
A-2-a	34	224	.1192	403	6125	15.2	125.5	460	1.298	157.0	1.25
A-3-a	27	241	.1254	408	6200	15.2	150.7	437.5	1.125	188.4	1.25
A-4-a	28	416	.2370	384	5920	15.4	207.1	231.5	1.073	235.1	1.135
A-5-a	30	600	.3613	374.5	5765	15.4	246.1	151.8	1.087	(a)	
B-4-a	32	310	.1787	385	5890	15.3	166.4	307	1.154	188.9	1.135
B-5-a	31	484	.2868	377	5805	15.4	188.5	191.5	1.272	226	1.20
A-2-b	36	226	.1190	405	6160	15.2	122.5	461.5	1.335	144.6	1.18
A-2-c	37	203	.1066	407	6180	15.2	119.3	514.6	1.304	139.5	1.17
C-1-a	33	489	.2899	377	5805	15.4	121.8	169	2.091	144.3	1.185
C-1-b	35	514	.2939	384	5910	15.4	119.3	167	2.190	(a)	

[a]No flutter.

TABLE III.- STEADY AERODYNAMIC COEFFICIENTS

	Theoretical values for $\alpha = 4^\circ$ (0.06981 rad)	Experimental values for -		Difference between theoretical and experimental values for $\alpha = 4^\circ$, percent of experimental value
		$\alpha = 4^\circ$	$\alpha = 10^\circ$	
C_L	[a]0.00798			
C_{L_α}, per rad	0.1143			
q, lb/sq in.	4.02			
l_M^2, in.^{2}	441			
l_F, in.	18			
C_A		0.0030	0.0034	
C_l		0	0.0010	
C_N	0.0080	0.0086	0.0248	-7.0
C_m	0.00427	0.00514	0.01528	-17.0
x_{ac}	0.534	0.597	0.617	-10.6

[a] $C_L = \alpha C_{L_\alpha}$.

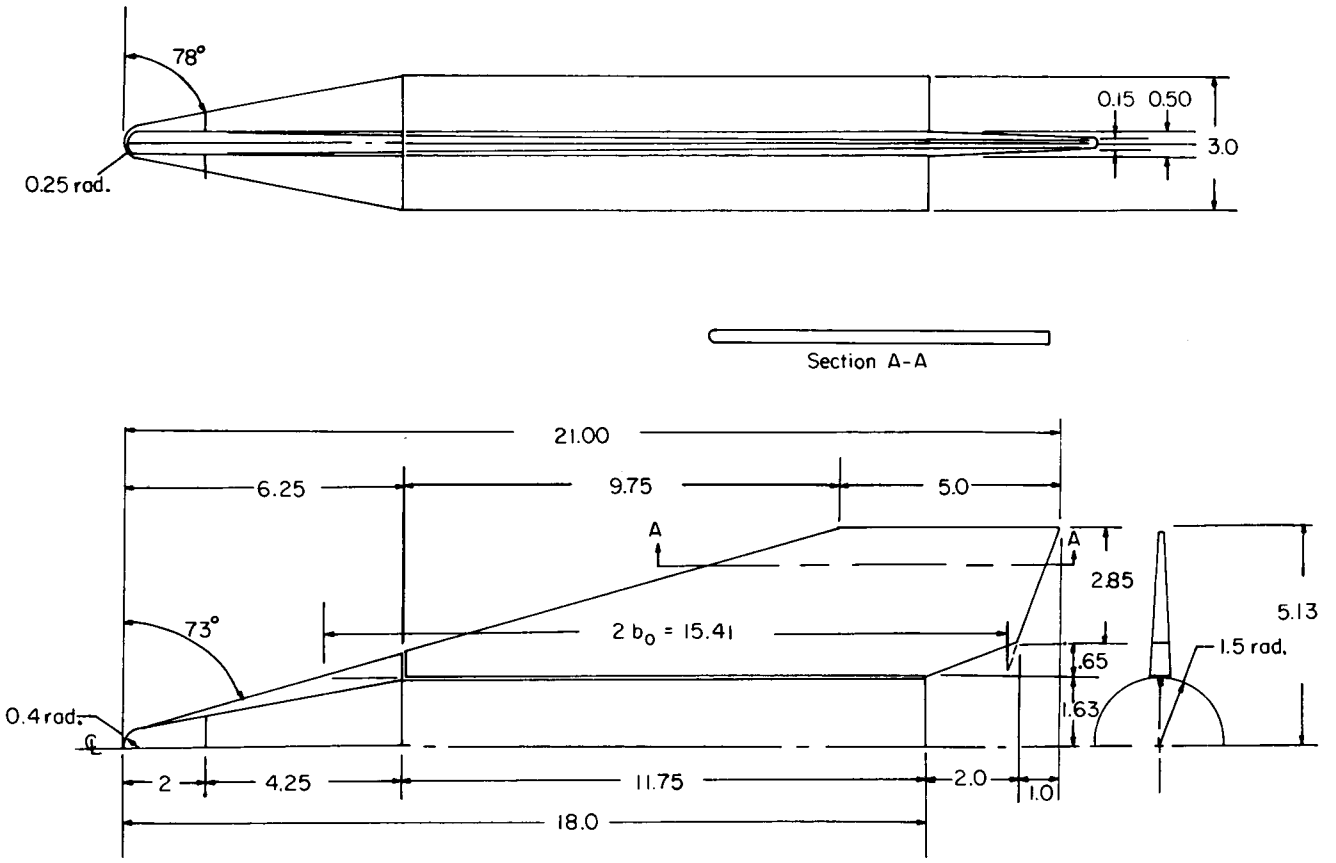

Figure 1.- Model geometry. Linear dimensions are in inches.

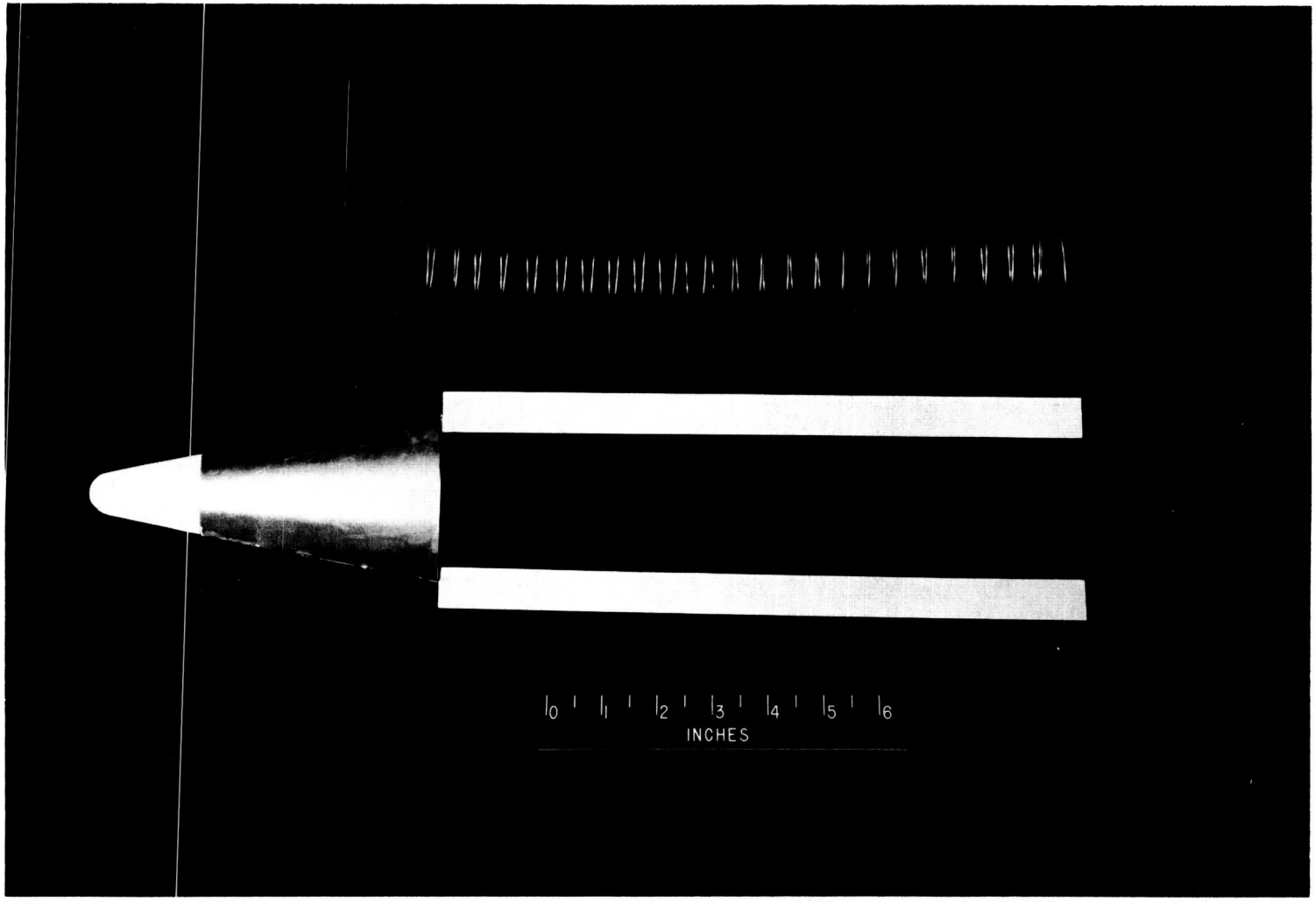

(a) Cone and integral longitudinal inserts with unmounted coil spring. L-64-3338

Figure 2.- Model construction.

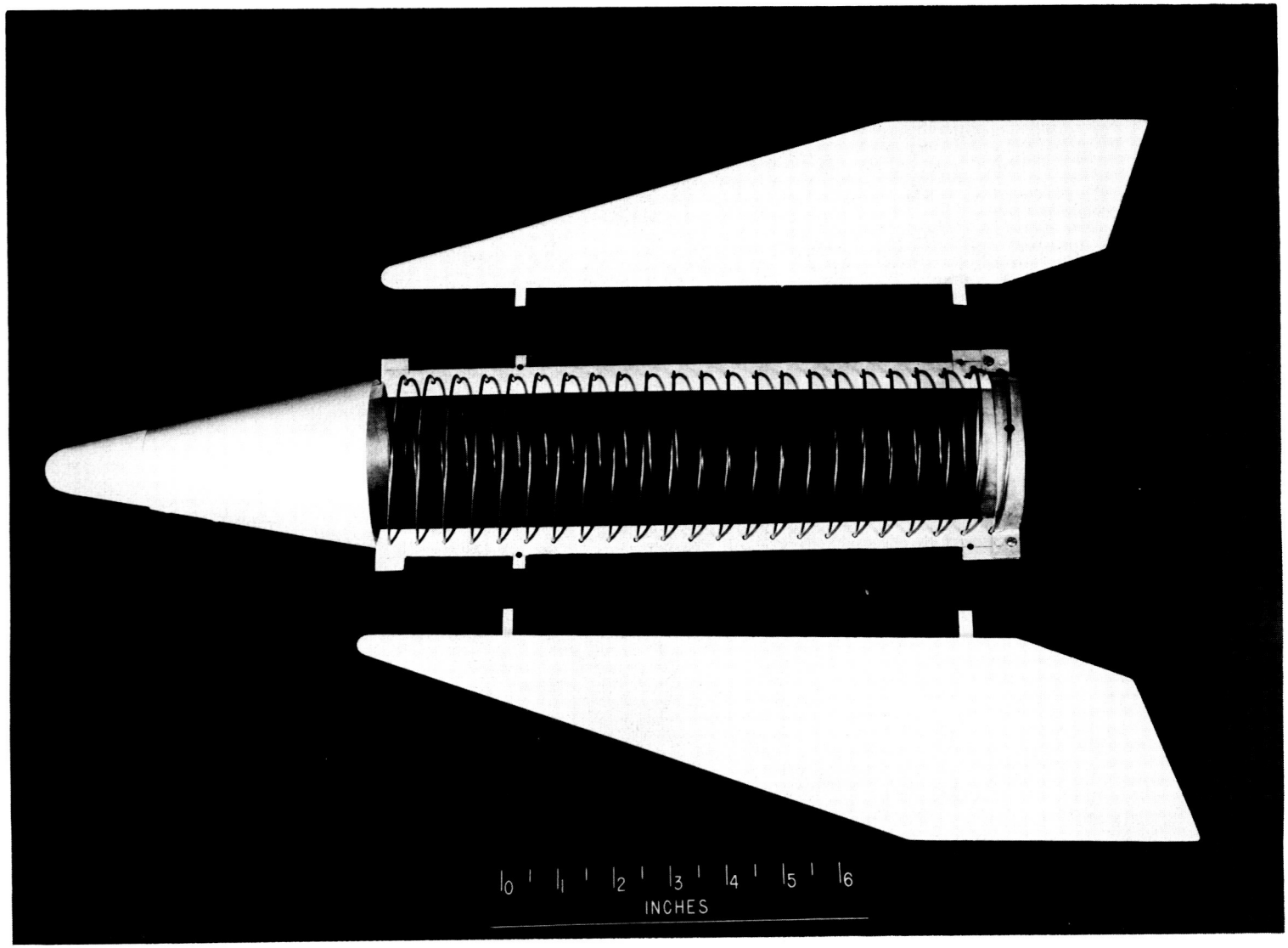

(b) Model with coil spring mounted and wings unmounted. L-64-3339

Figure 2.- Continued.

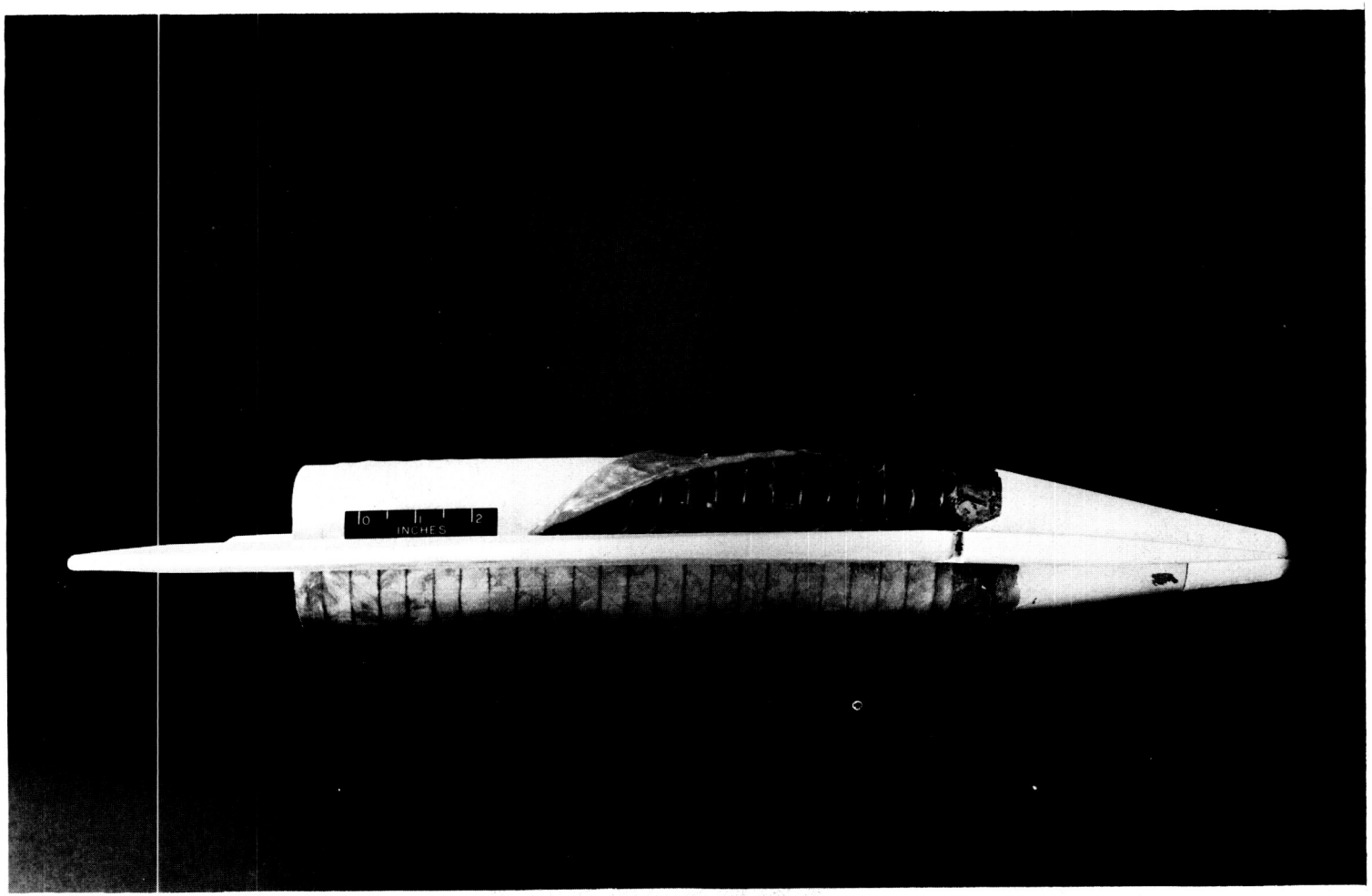

(c) Side view of model with wings mounted and rubber covering partially installed on fuselage. L-64-3335

Figure 2.- Continued.

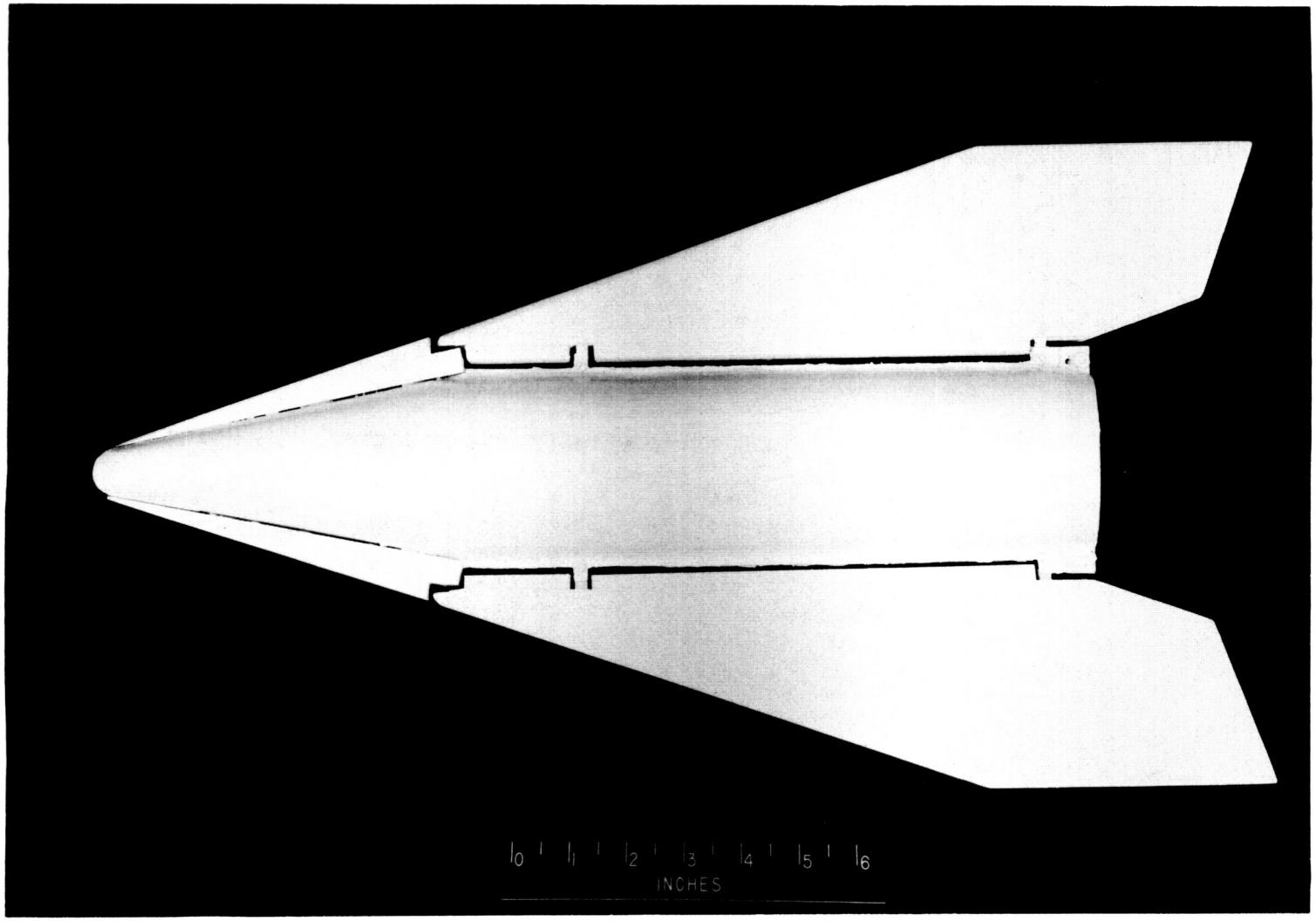

(d) Top view of finished model. L-64-3340

Figure 2.- Continued.

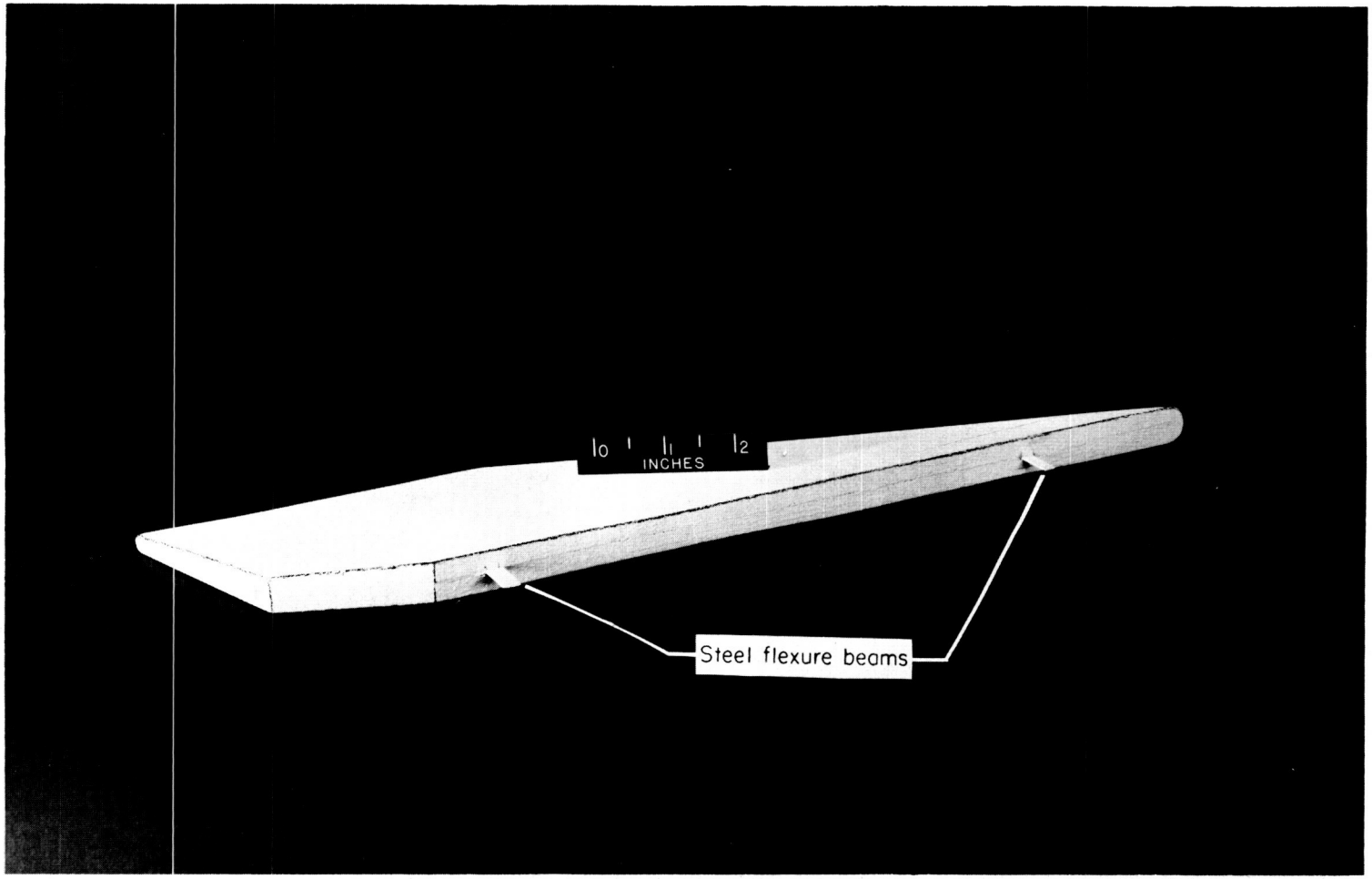

(e) View of wing showing root chord and trailing edge. L-64-3336.1

Figure 2.- Continued.

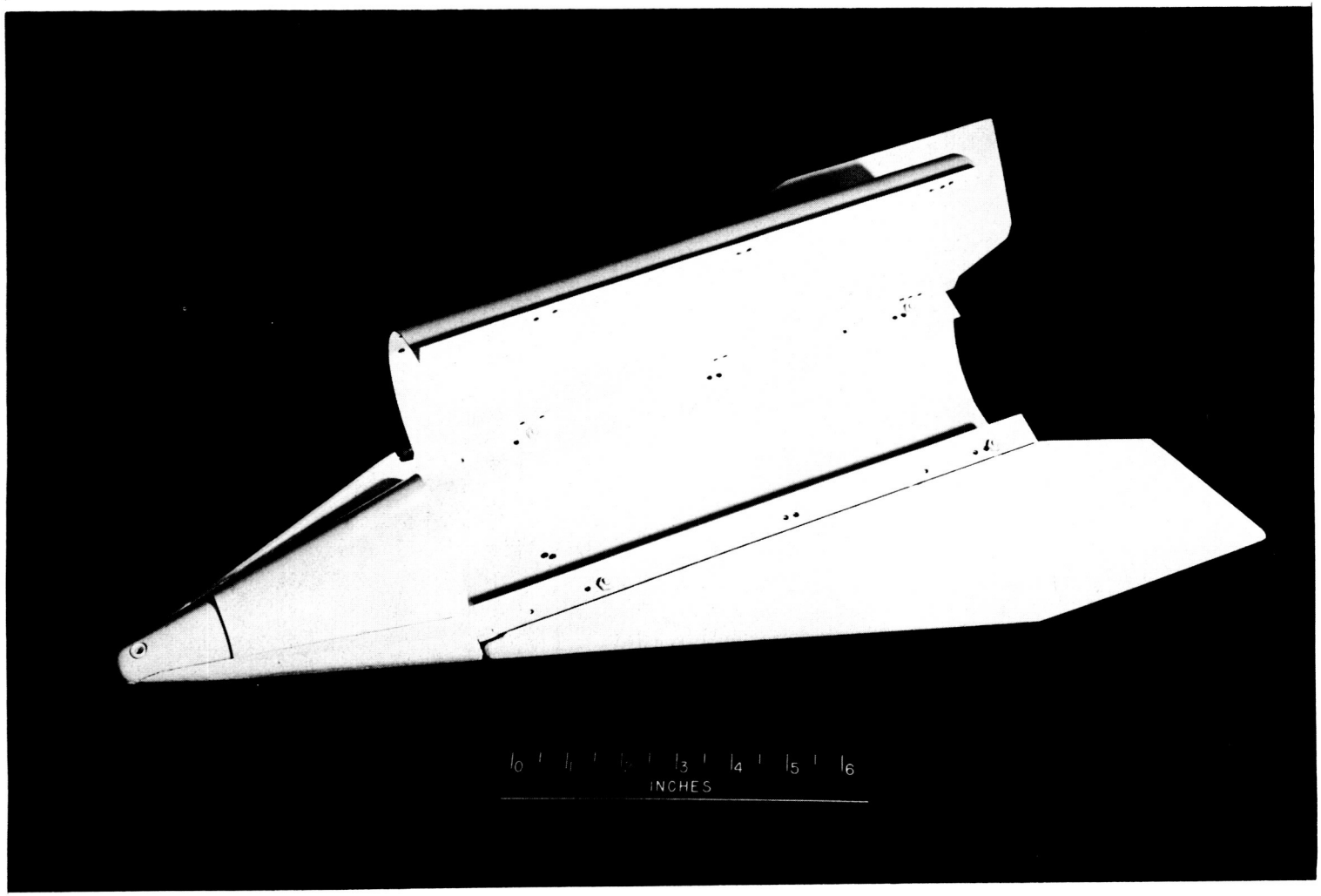

(f) Rigid-fuselage model with upper portion of cylindrical fuselage rotated out of place. L-64-3337

Figure 2.- Concluded.

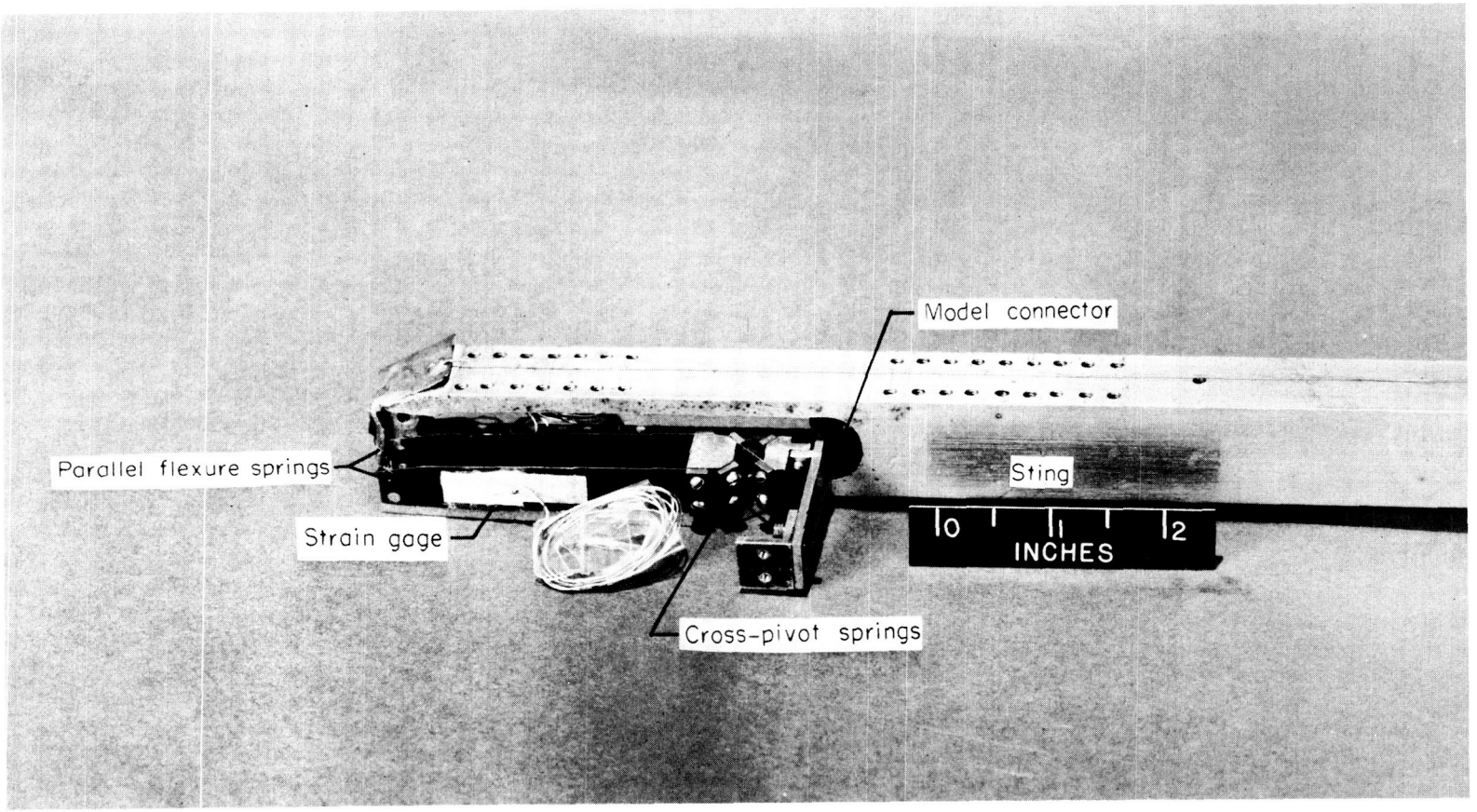

Figure 3.- Model support system.

L-64-3343.1

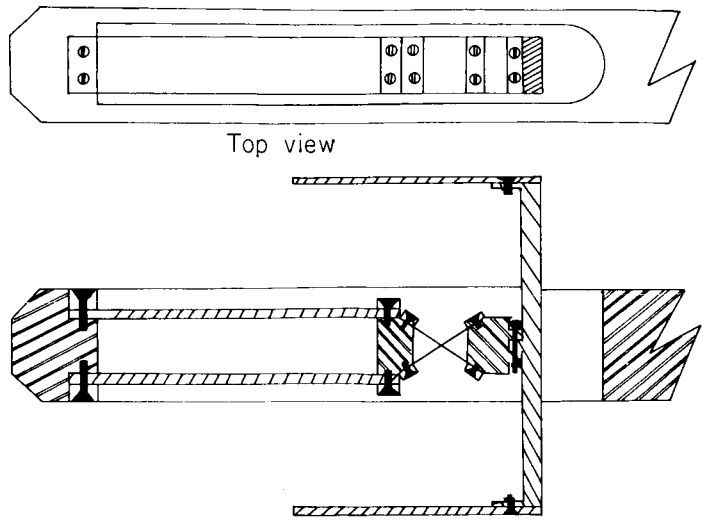

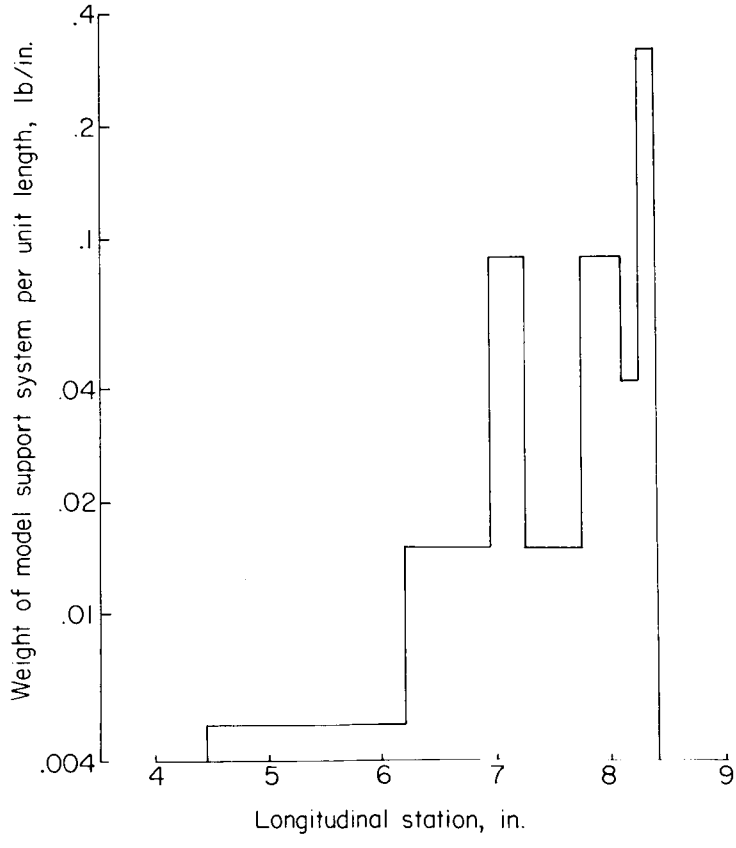

(a) Model support system.

Figure 4.- Weight distributions.

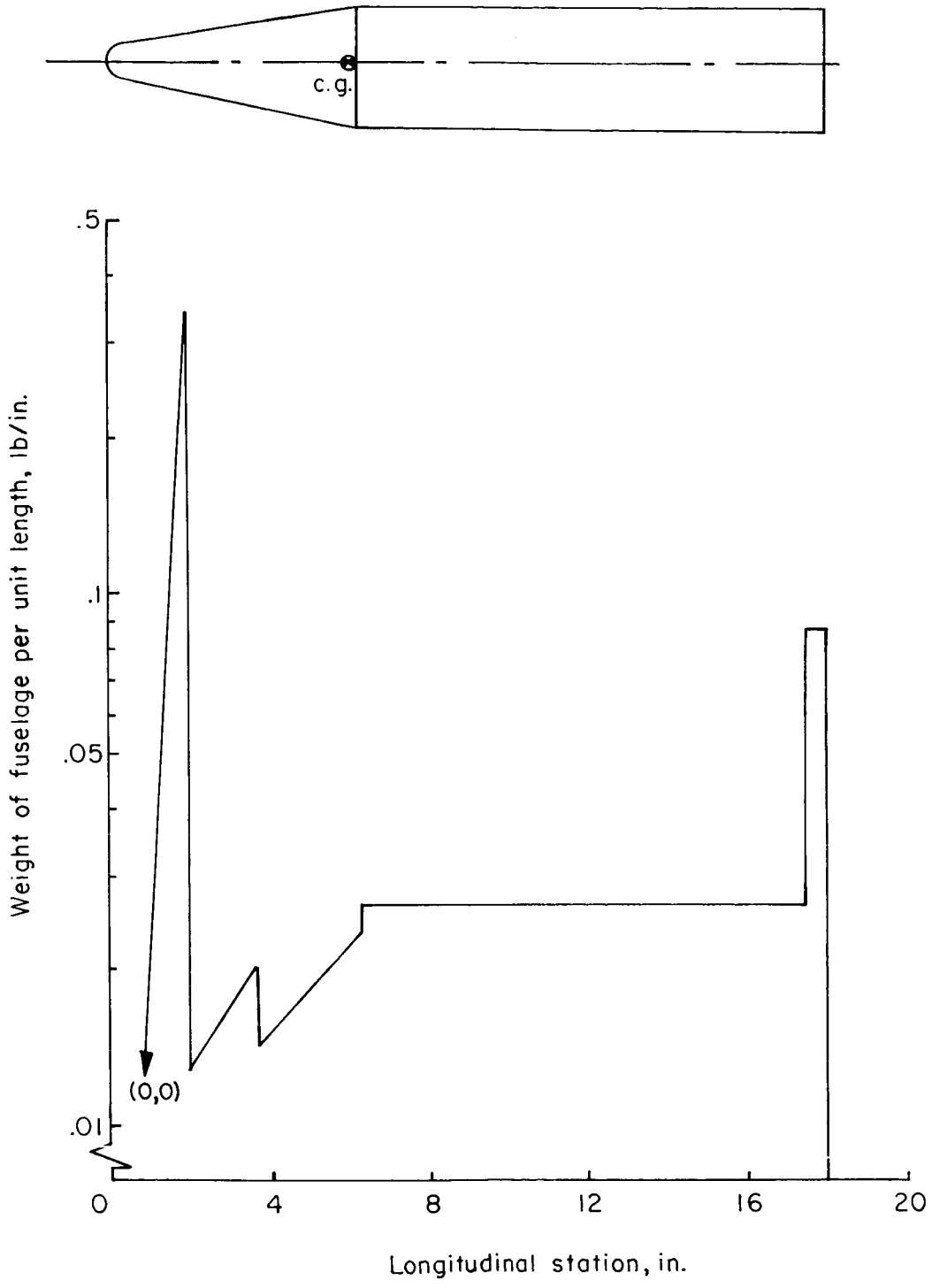

(b) Typical flexible fuselage.

Figure 4.- Continued.

Wing — flapping-stiffness level	Concentrated mass due to flexure-beam weight, lb, at —					
	x = 8.5 in.		x = 17.5 in.			
	◇	△	○	□	◇	△
1	0.00025	0.00051	0.00087	0.00087	0.00087	0.00087
3	.00034	.00067	.00110	.00108	.00108	.00108
4	.00042	.00064	.00135	.00135	.00135	.00135
5	.00052	.00102	.00173	.00173	.00173	.00173

Spanwise station, in.
—○— 1.5
--□-- 2.5
--◇-- 3.5
--△-- 4.5

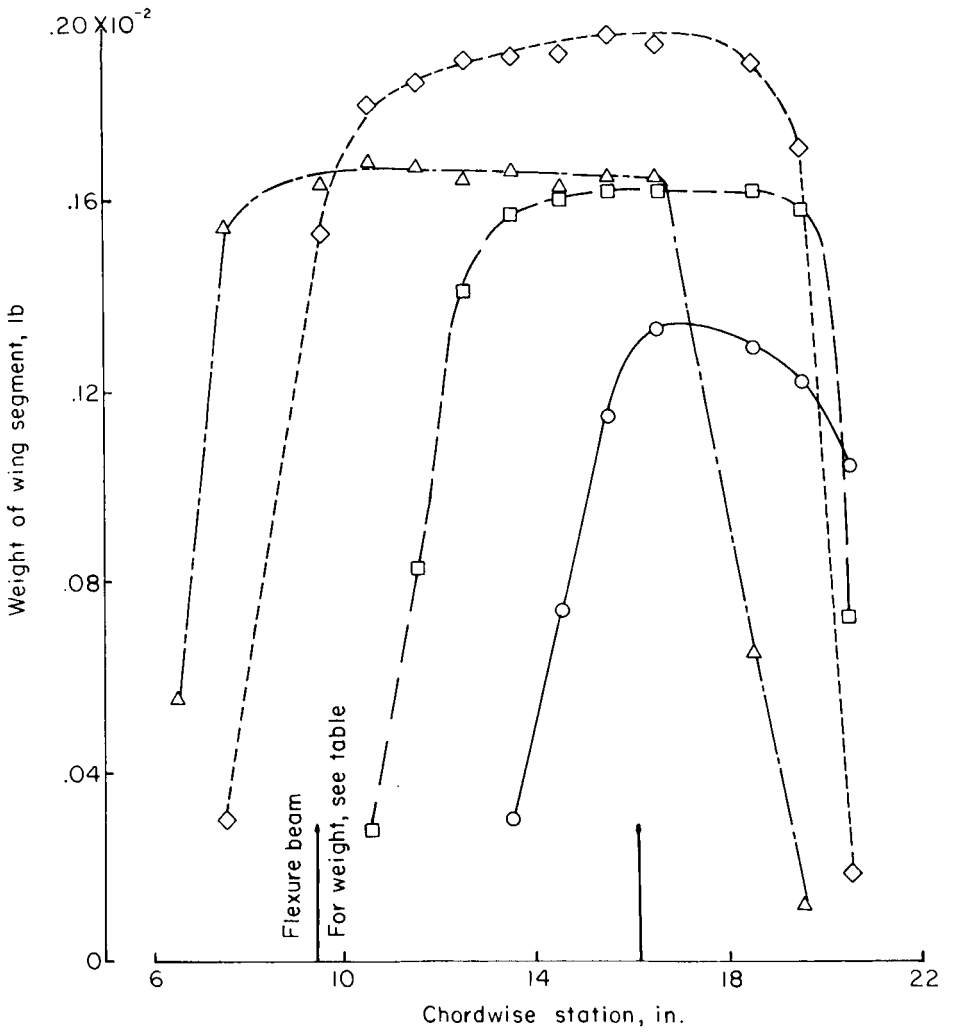

(c) One wing.

Figure 4.- Concluded.

Fuselage	Fraction of fuselage length from center of gravity to—	
	Aerodynamic center	Pitch axis
Rigid	0.1946	0.0986
Flexible	.1446	.0480

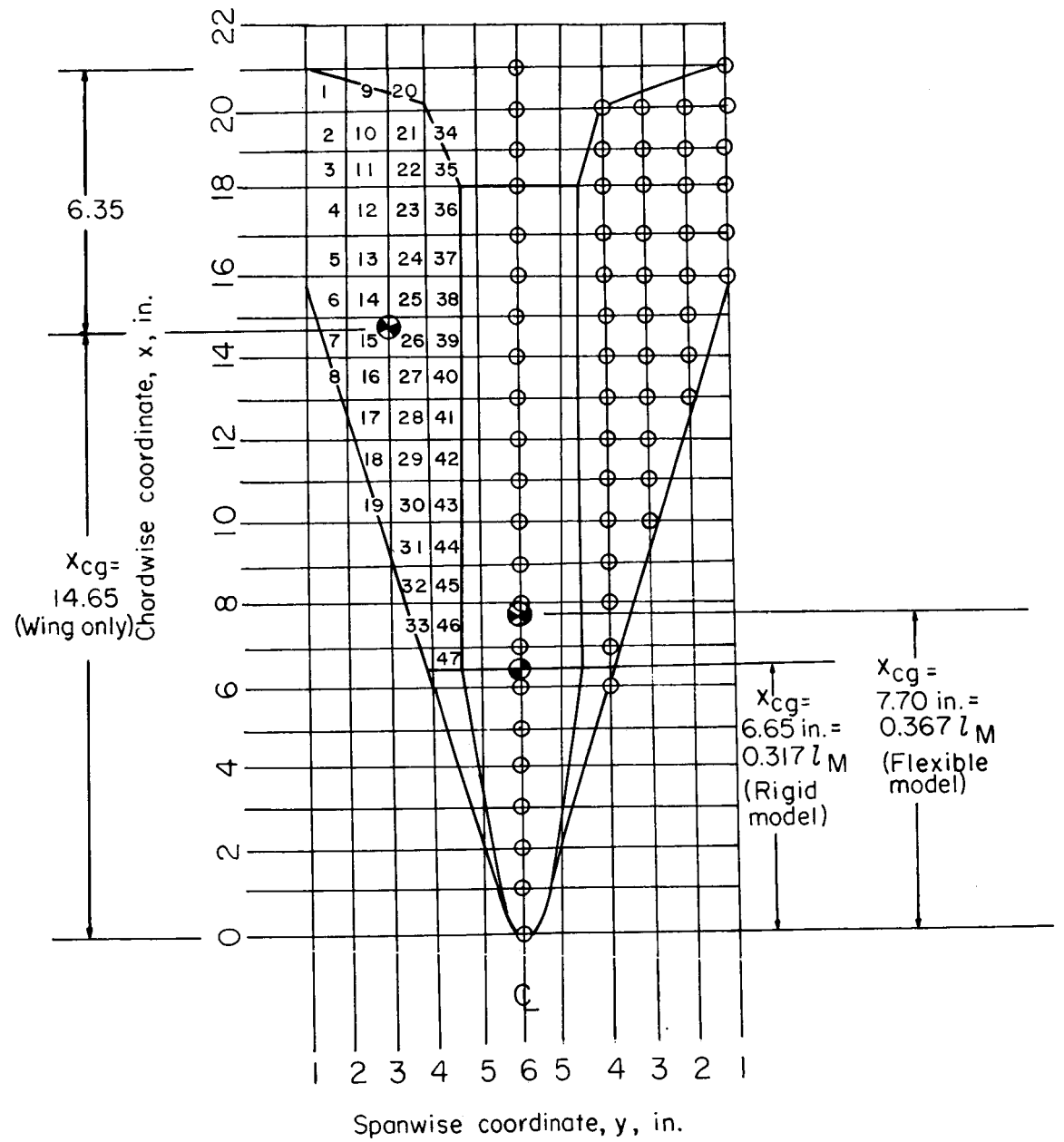

Figure 5 - Coordinate system and model center-of-gravity location.

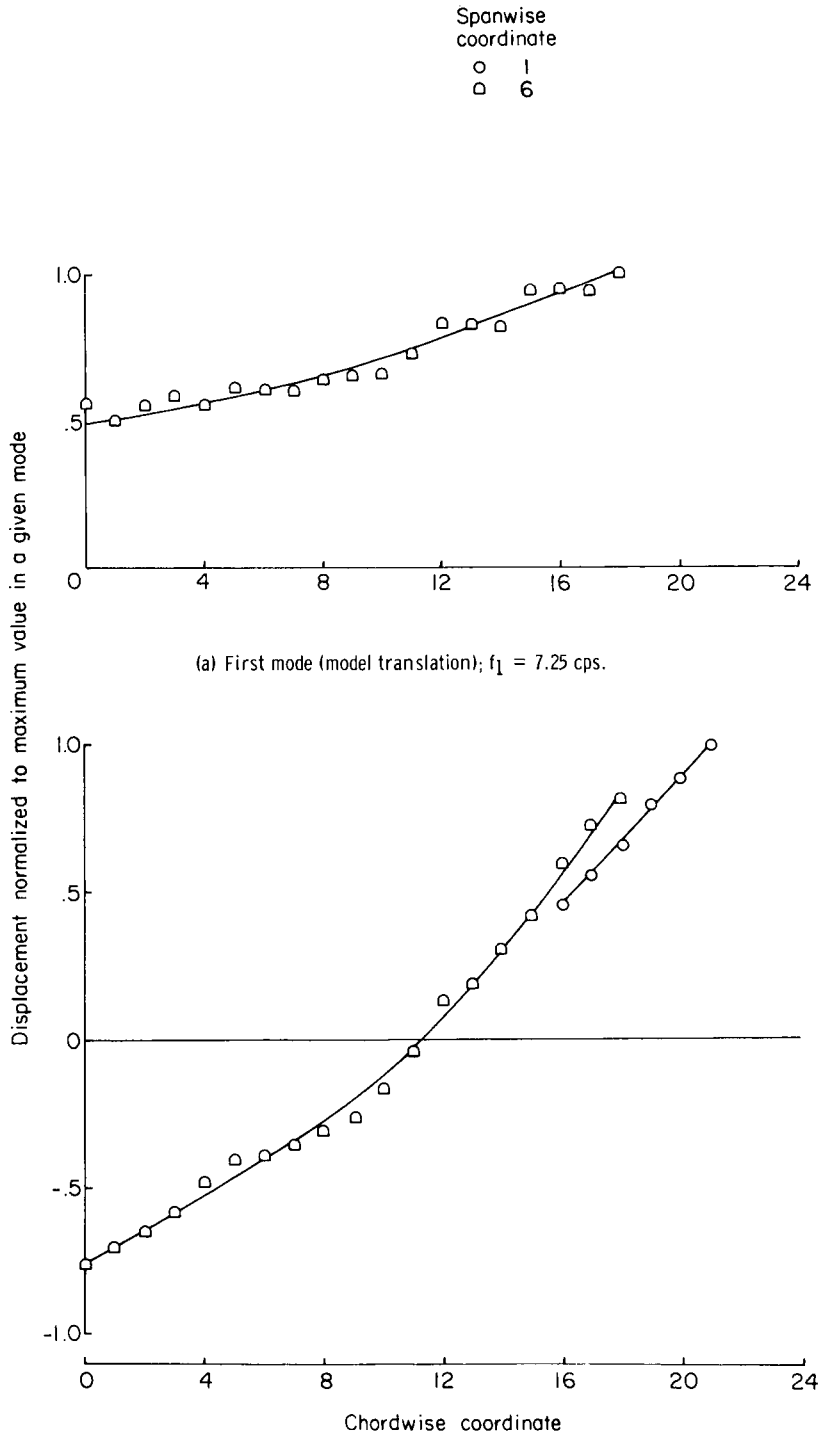

(a) First mode (model translation); f_1 = 7.25 cps.

(b) Second mode (model pitch); f_2 = 10.50 cps.

Figure 6.- Mode shapes for model A-2-a.

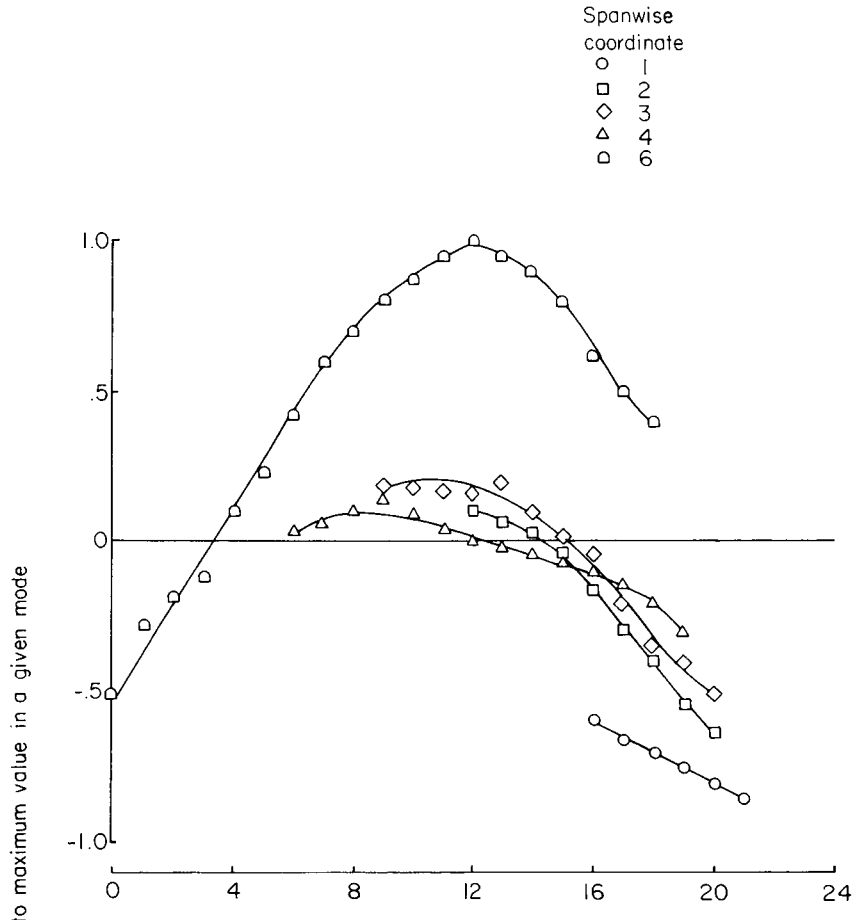

(c) Fourth mode (fuselage bending); f_4 = 25.00 cps.

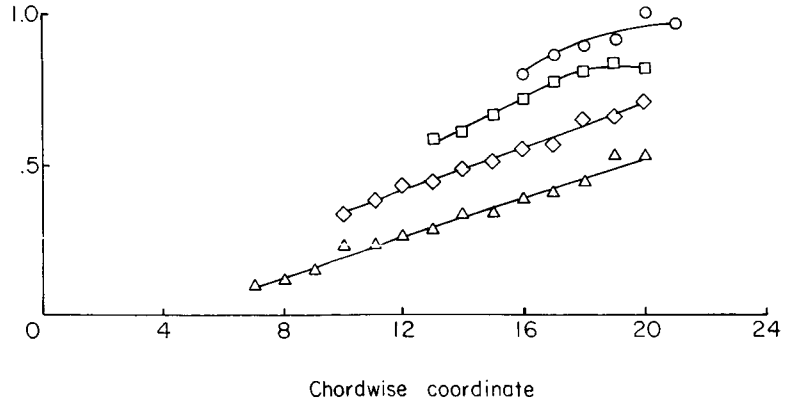

(d) Uncoupled wing flapping mode (fuselage restrained); f_W = 20.0 cps.

Figure 6.- Continued.

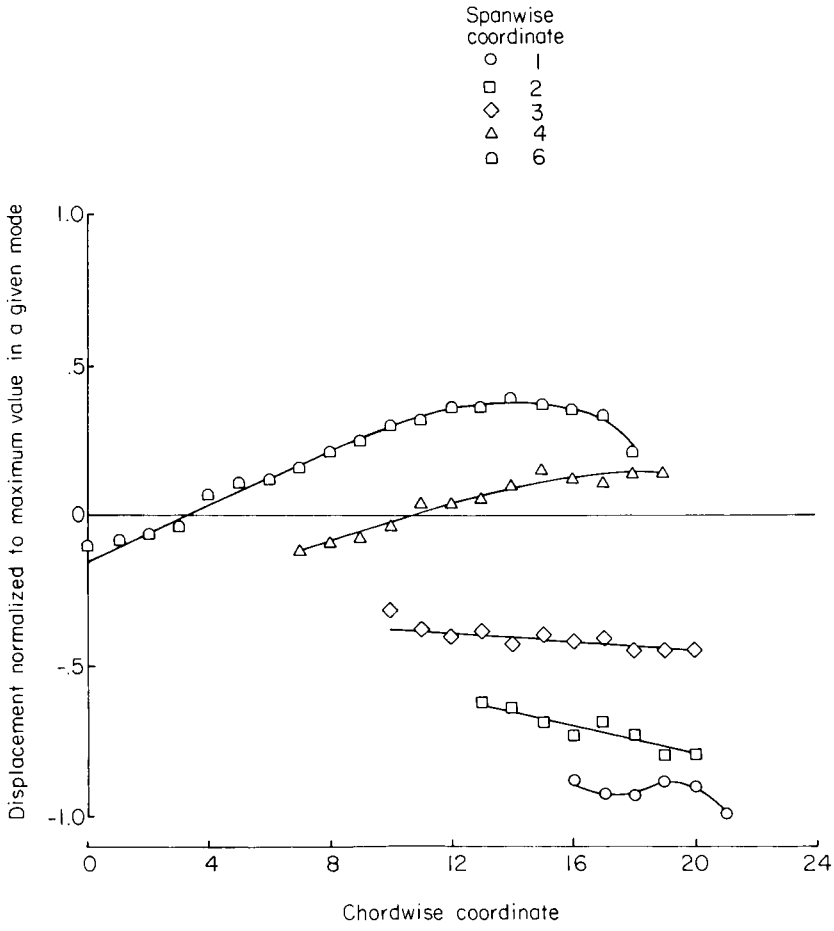

(e) Fifth mode (wing-fuselage combination); f_5 = 29.0 cps.

Figure 6.- Concluded.

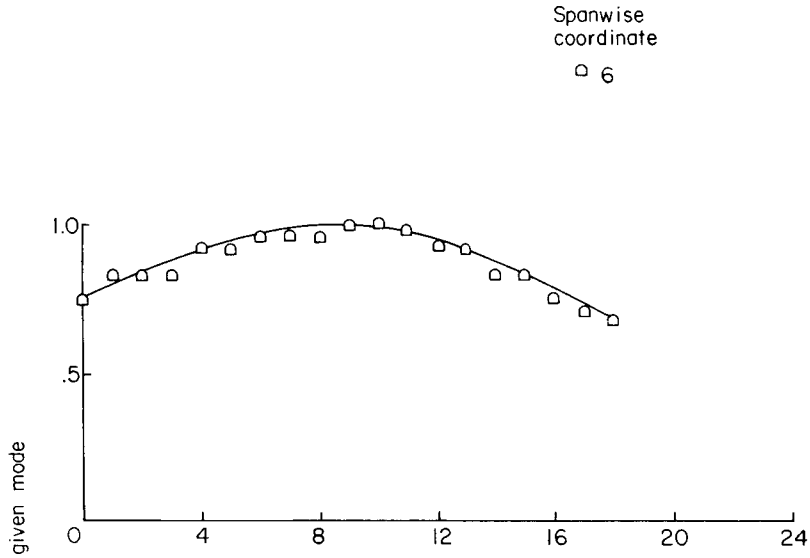

(a) First mode (model translation); f_1 = 7.10 cps.

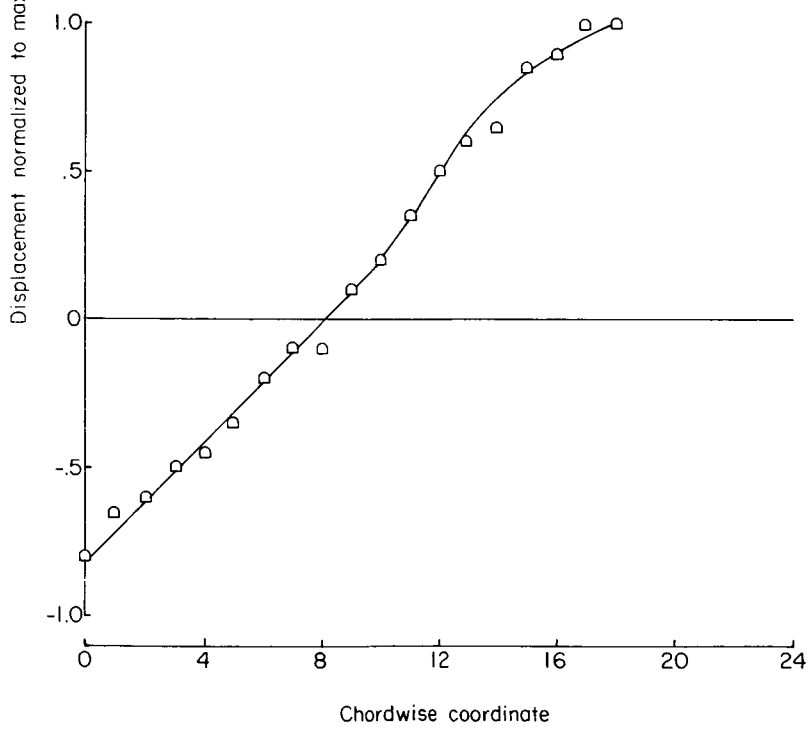

(b) Second mode (model pitch); f_2 = 10.7 cps.

Figure 7.- Mode shapes for model B-4-a.

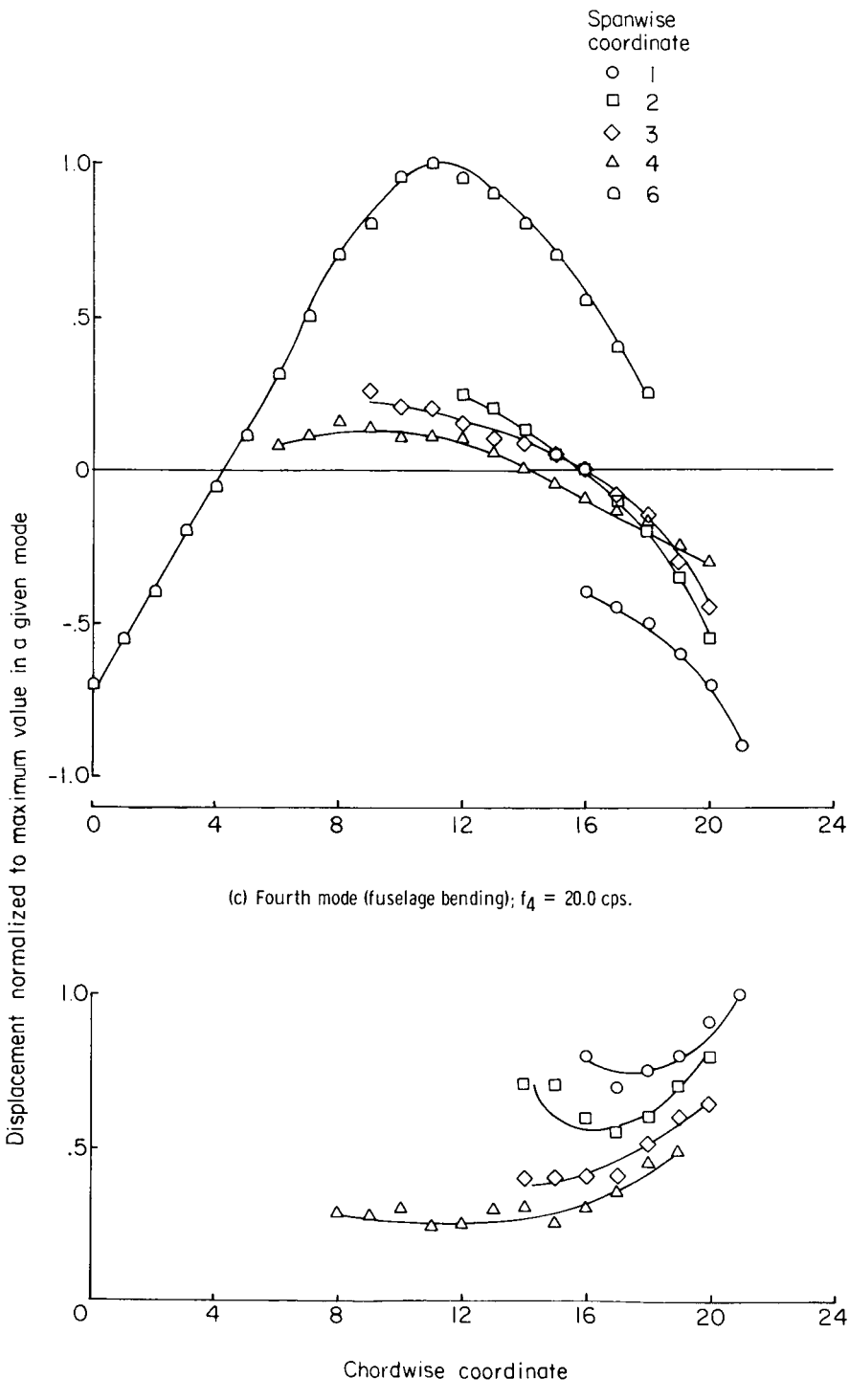

(c) Fourth mode (fuselage bending); f_4 = 20.0 cps.

(d) Uncoupled wing flapping mode (fuselage restrained); f_W = 26.50 cps.

Figure 7.- Continued.

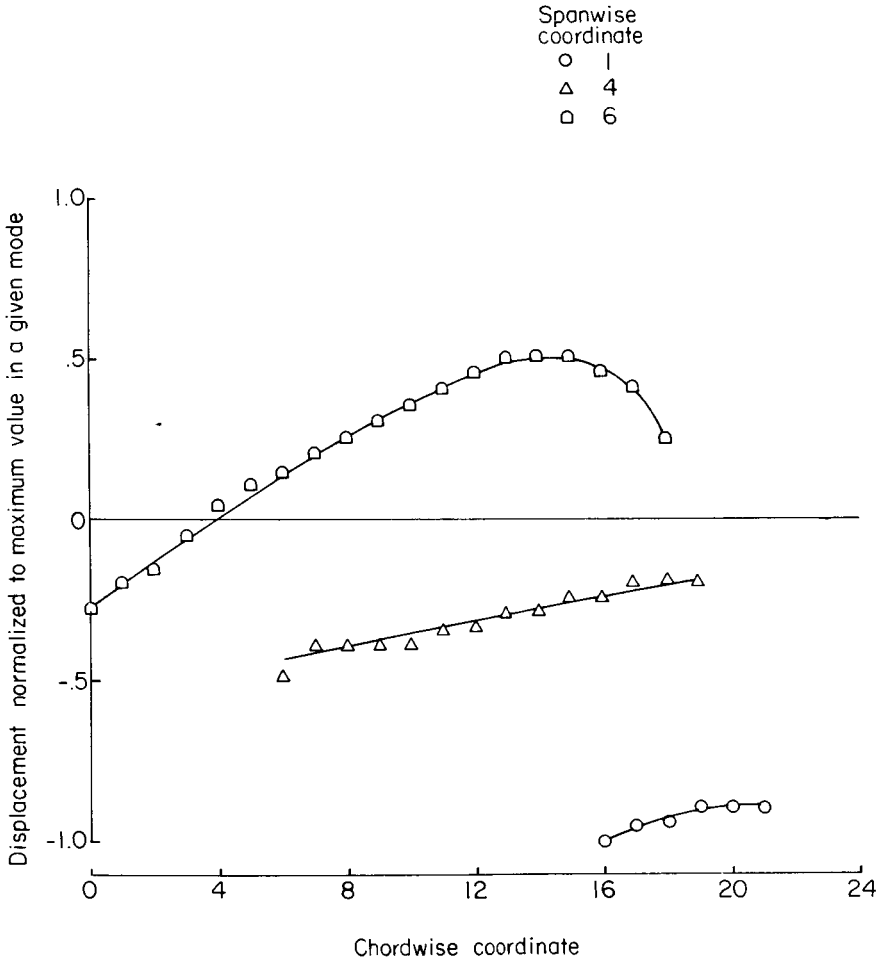

(e) Fifth mode (wing-fuselage combination); f_5 = 31.00 cps.

Figure 7.- Concluded.

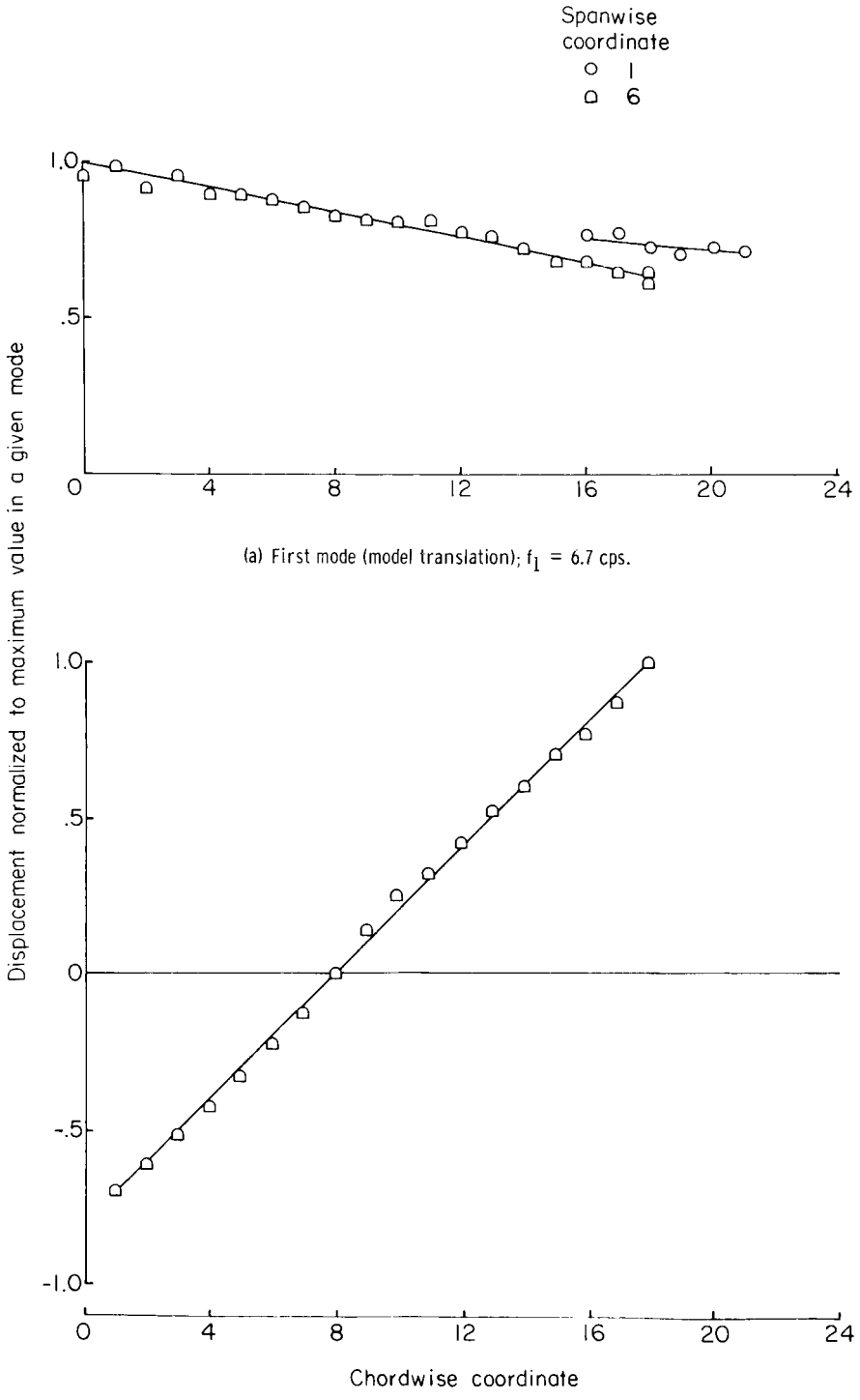

(a) First mode (model translation); f_1 = 6.7 cps.

(b) Second mode (model pitch); f_2 = 11.0 cps.

Figure 8.- Mode shapes for model C-1-a.

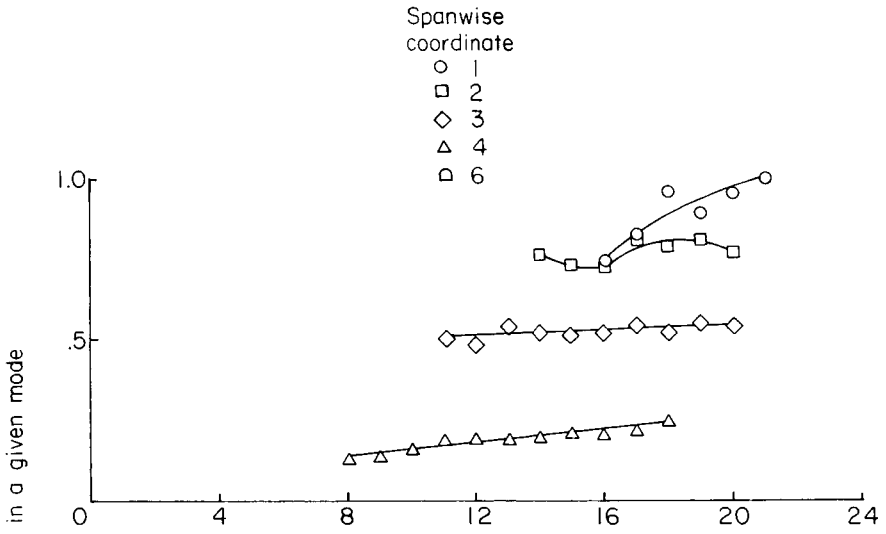

(c) Uncoupled wing flapping mode (fuselage restrained); f_W = 19.40 cps.

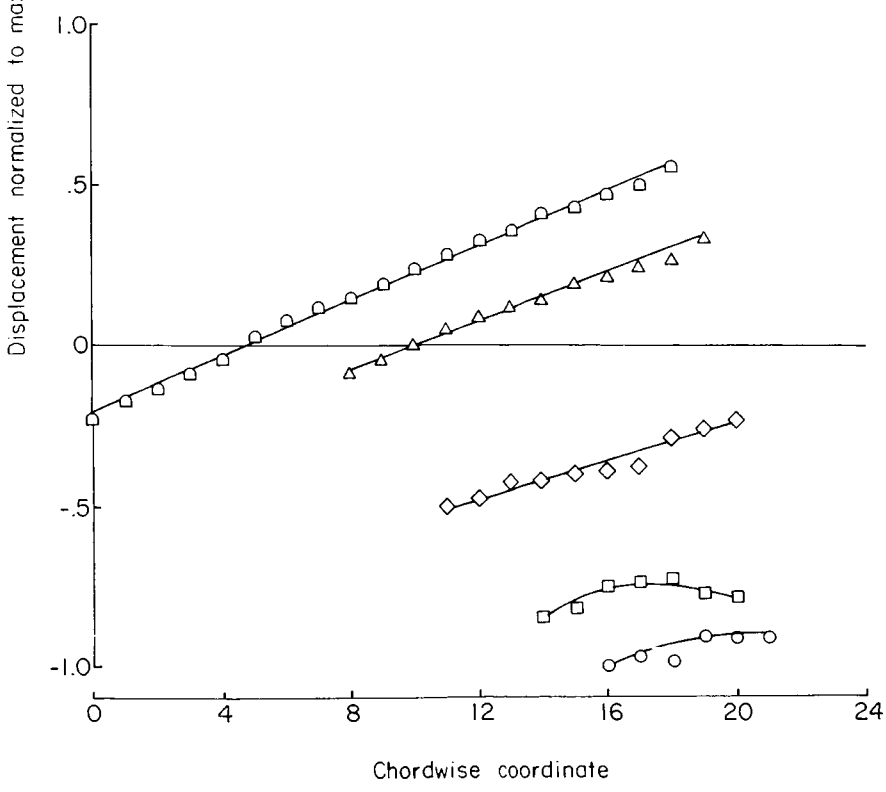

(d) Fifth mode (wing fuselage combination); f_5 = 24.00 cps.

Figure 8.- Concluded.

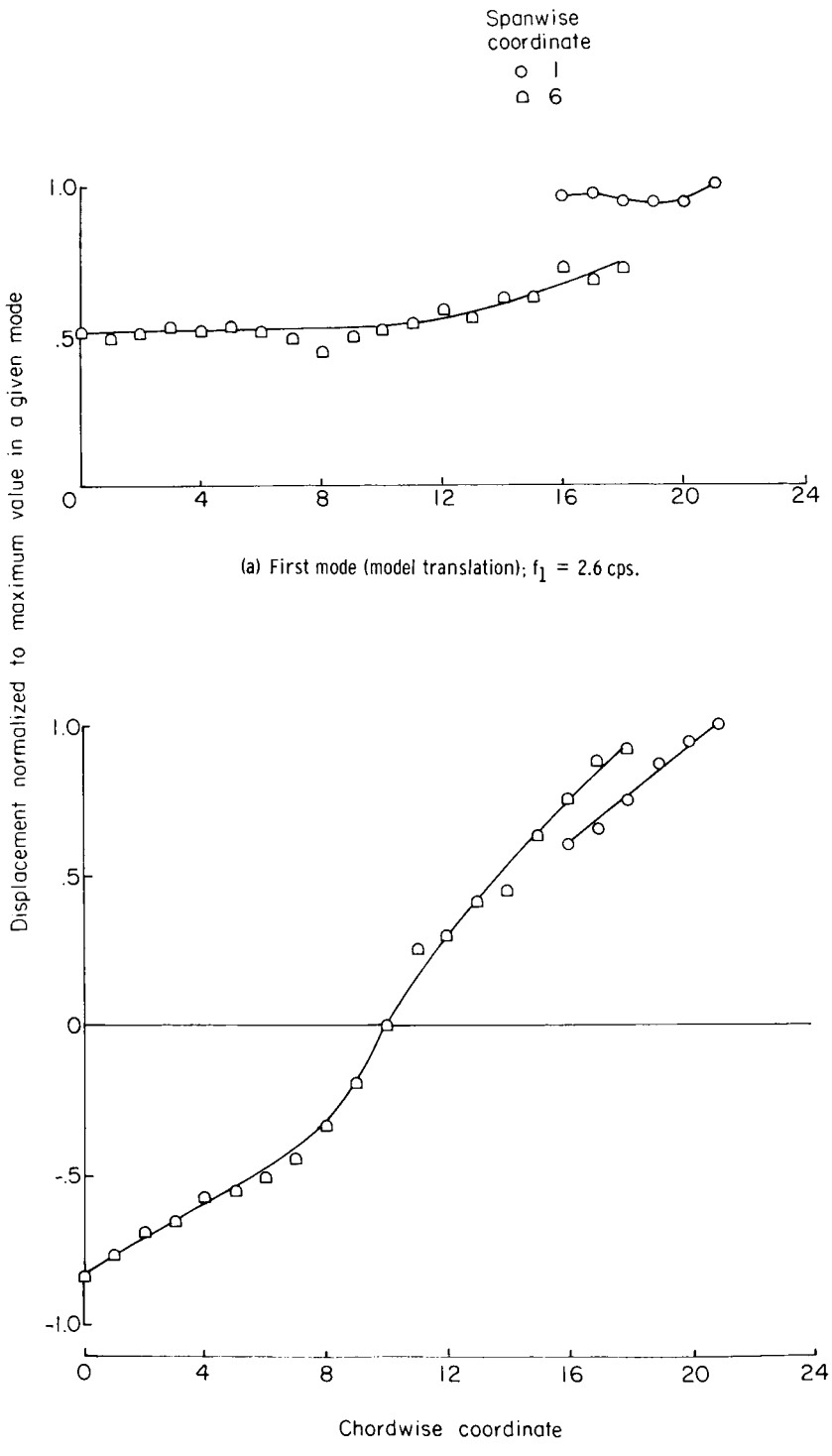

(a) First mode (model translation); f_1 = 2.6 cps.

(b) Second mode (model pitch); f_2 = 4.0 cps.

Figure 9.- Mode shapes for model A-2-c.

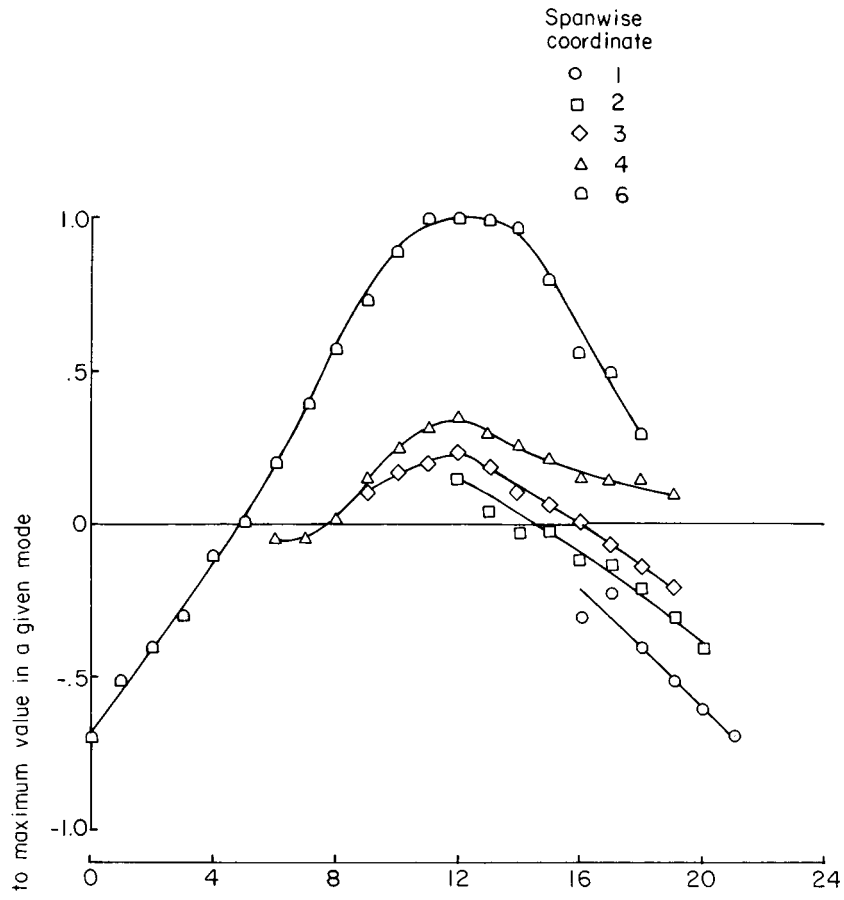

(c) Fourth mode (fuselage bending); f_4 = 24.0 cps.

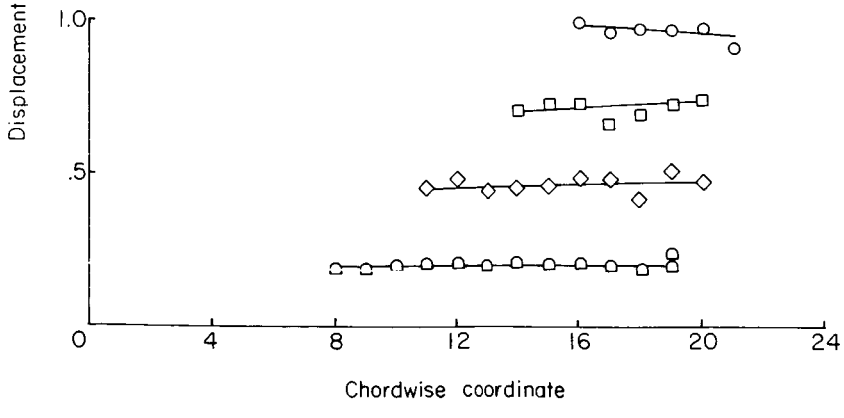

(d) Uncoupled wing flapping mode (fuselage restrained); f_W = 19.0 cps.

Figure 9.- Continued.

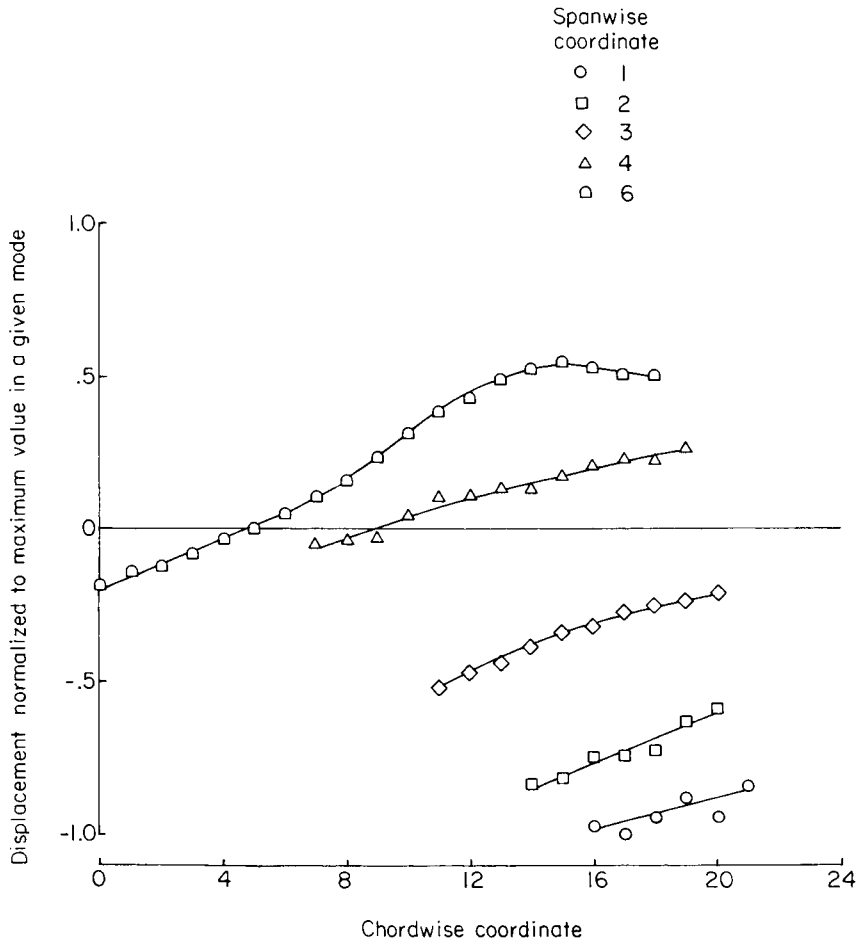

(e) Fifth mode (wing-fuselage combination); f_5 = 27.0 cps.

Figure 9.- Concluded.

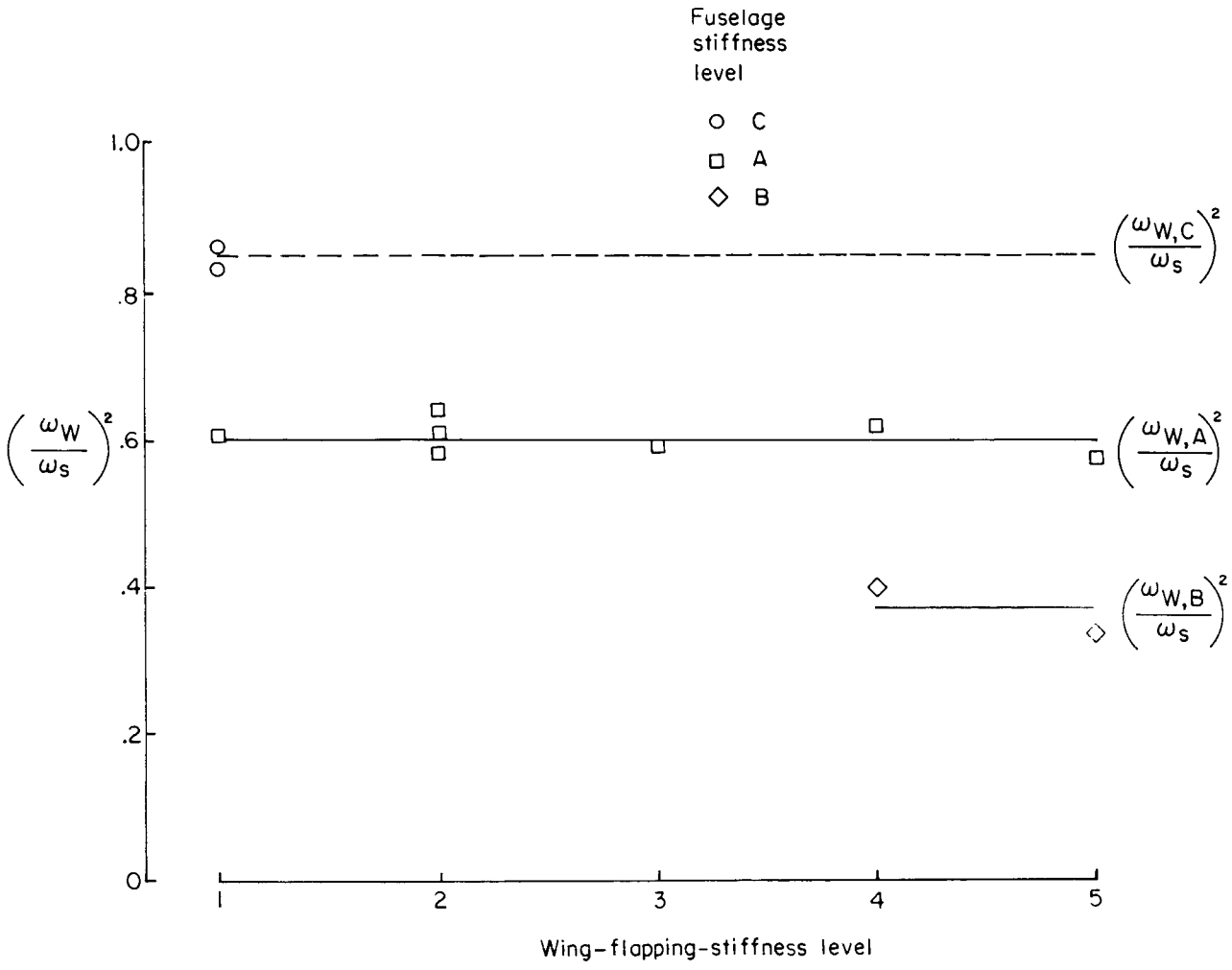

Figure 10.- Reduction in wing-flapping-stiffness ratio due to flexible wing-fuselage junction for various models.

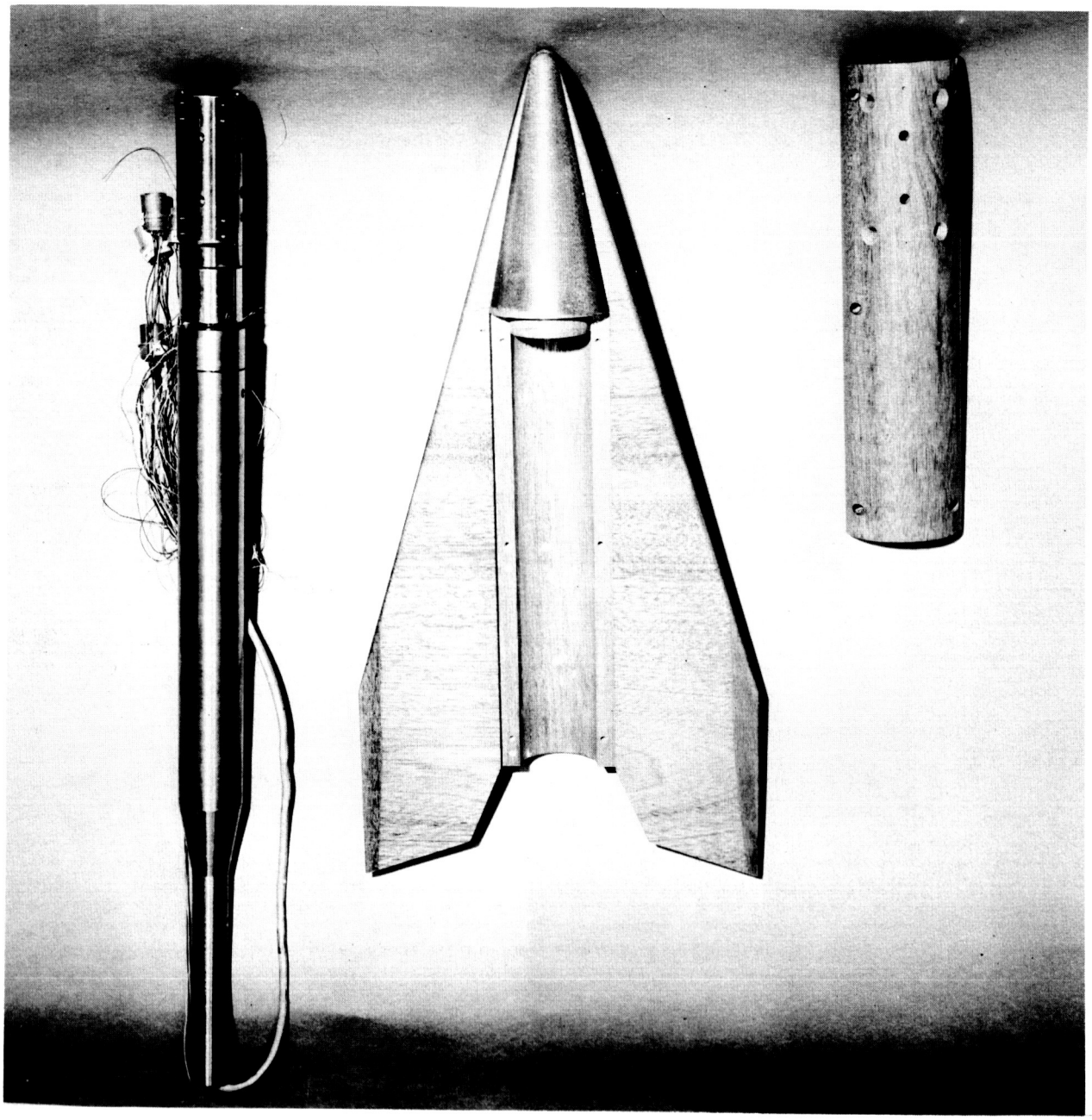

Figure 11.- Aerodynamic-force model and strain-gage balance. L-63-3789.1

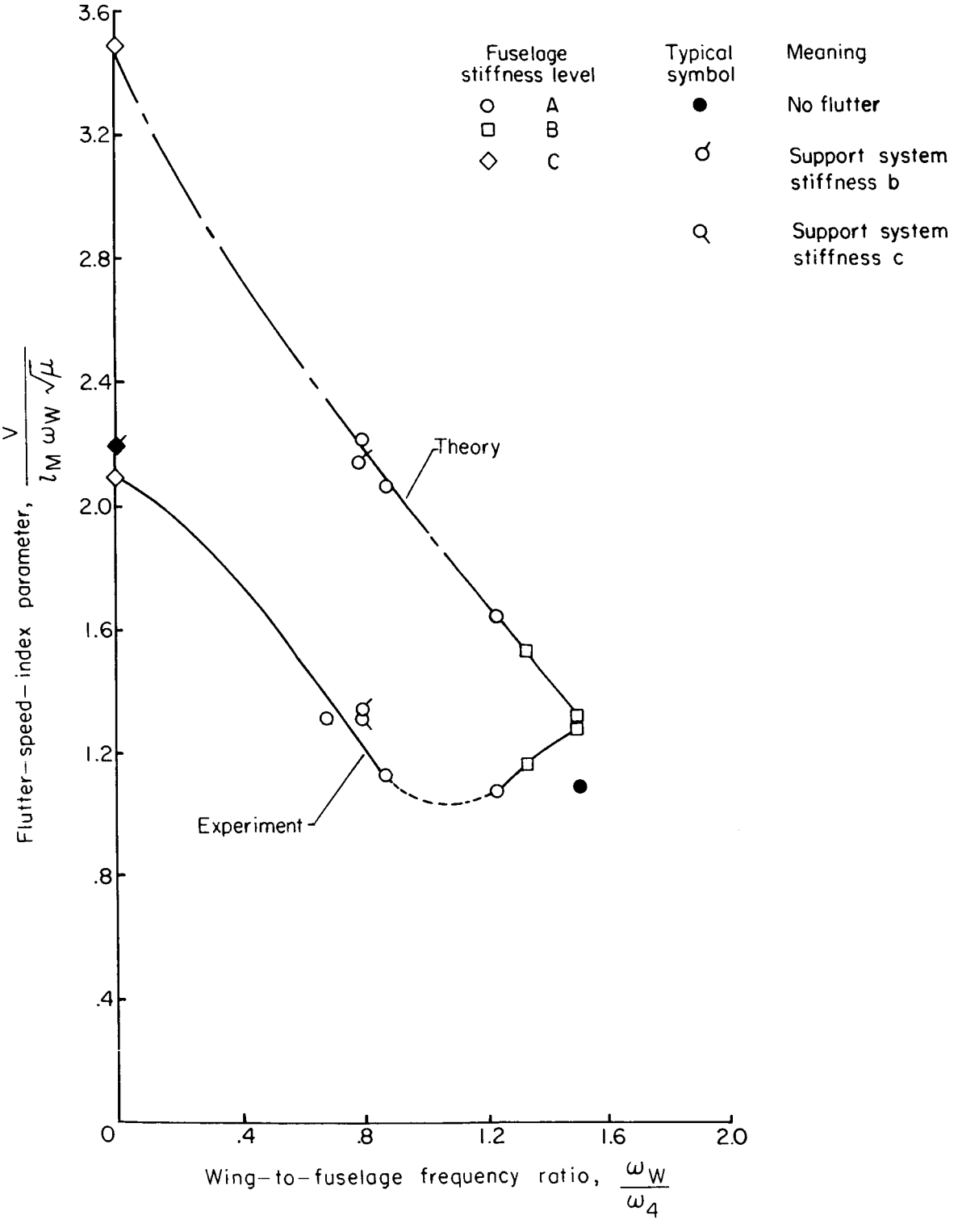

Figure 12.- Variation of flutter speed with wing-fuselage frequency ratio.

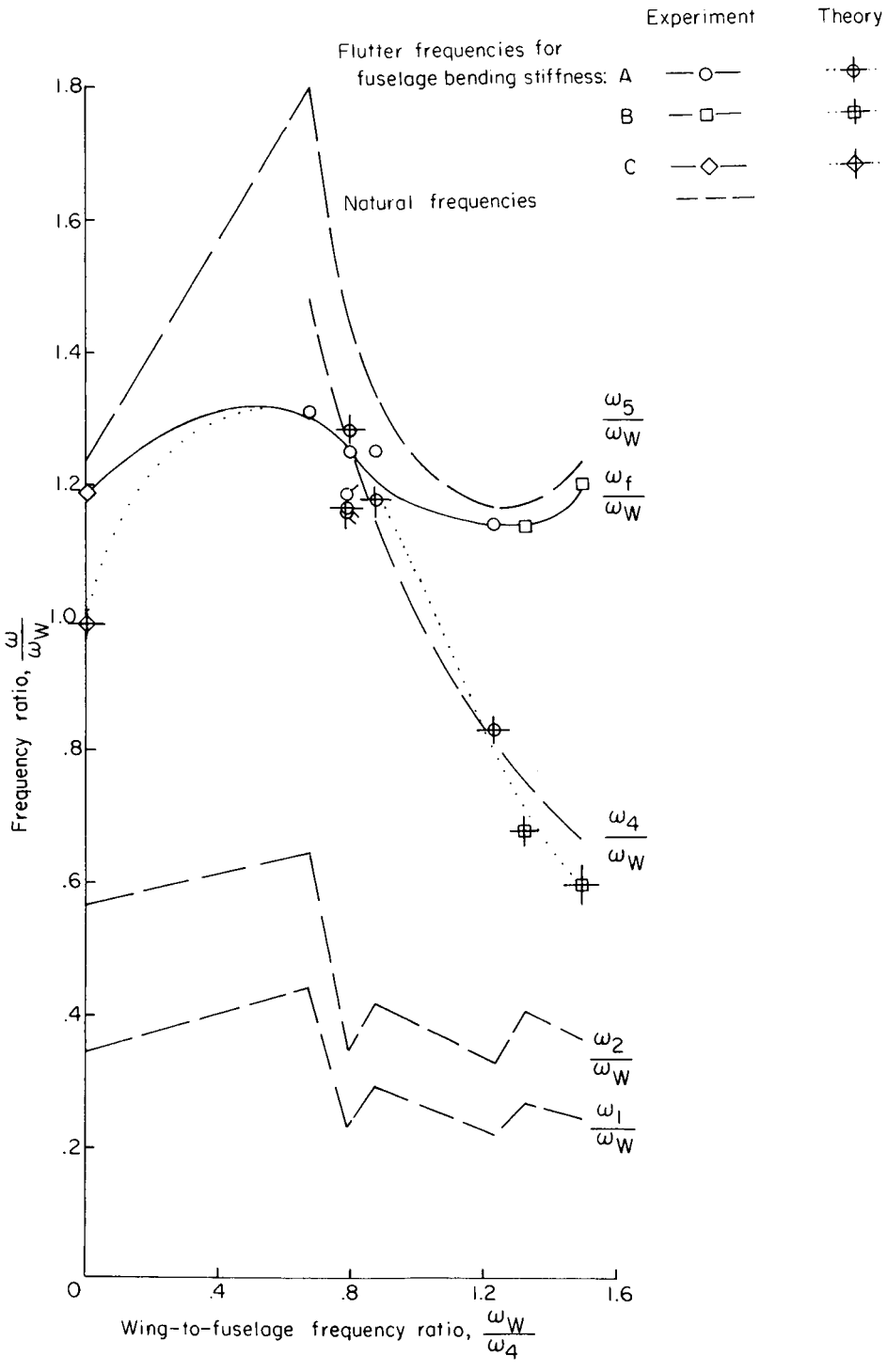

Figure 13.- Variation of frequency ratios ω/ω_W with wing-to-fuselage frequency ratio. The symbols with flags represent data obtained at stiffness level b and the symbols with tails, data obtained at stiffness level c.

NASA-Langley, 1965 L-4328